OPTICAL SCIENCES CENTER

TECHNICAL MEMORANDUM 3

FINAL POSTFLIGHT CALIBRATION REPORT ON APOLLO 9 MULTIBAND PHOTOGRAPHY EXPERIMENT SO65

R. A. Schowengerdt
P. N. Slater

May 1972

FINAL POSTFLIGHT CALIBRATION REPORT ON APOLLO 9 MULTIBAND PHOTOGRAPHY EXPERIMENT SO65

R. A. Schowengerdt
P. N. Slater

Optical Sciences Center
University of Arizona
Tucson, Arizona 85721
May 1972

ABSTRACT

The Apollo 9 SO65 photography experiment was the first systematic attempt to gather photographic multispectral data from earth orbit. The quality of imagery supplied to the many users of this data is of considerable interest. We evaluated duplicates of the original film up to the fourth generation, compared the quality of the images in each wavelength band of the black-and-white film systems, and estimated the absolute resolution of one of the SO65 bands by comparing it to simultaneous aircraft photography.

Fourier analysis was applied to microdensitometer scans of a selected region of one SO65 frame in each of the three black-and-white bands. The approach was unique because we used a somewhat arbitrary section of the image and thus were not limited to available targets as in edge analysis. Comparison of duplicates and calculation of absolute SO65 MTF were done by applying linear systems theory to the spatial spectra of the image scans.

It was found that the duplication process is nonlinear and results in general amplification of spatial frequency modulation. However, the increase in modulation is offset by a corresponding increase in the granularity of the copies. For example, the density granularity in the three black-and-white bands (BB, CC, DD) increased by the following amounts between second and fourth generation duplicates:

Band	Increase in granularity
BB (green, Pan-X)	+54%
CC (ir, 5424)	+67%
DD (red, Pan-X)	+39%

The amount of increase seemed to be related to the initial granularity (e.g., the CC band used grainy black-and-white ir film whereas the other two were on Pan-X), but a direct relationship was not verified.

Band-to-band comparison of image quality was achieved in the form of signal-to-noise ratio curves as a function of spatial frequency for each band. From this standpoint the DD band was an order of magnitude better than the other two. The average signal-to-noise values between 0 and 10 cycles/mm were about

Band	Average signal-to-noise (0 to 10 cycles/mm)
BB	1.0
CC	2.2
DD	47.0

The BB band was low because of high atmospheric luminance contributing to the image background at the shorter wavelengths used for this band, and the CC band was low because of the grainy nature of the ir-sensitive film. It should be kept in mind that only one scan was done in one frame of the SO65 photography and that quantities like signal-to-noise ratio will vary with the nature of the object.

The low signal-to-noise values for the BB and CC bands prevented estimation of the system MTF in these bands. However, the MTF for the DD band was calculated. After dividing this curve by the film MTF, a three-bar resolution value was estimated by applying the aerial image modulation (AIM) curve for the same film. The resulting limiting resolution value for the DD band was approximately 20 lp/mm.

There were several factors that restricted the analysis of the Apollo 9 imagery. Among these were the lack of precise sensitometric and optical system data on the high-altitude photography. In addition it was determined that there was only one simultaneous pair of high-altitude and SO65 frames. Finally, the original SO65 photography was not available for scanning (for obvious reasons), thus eliminating a reference base for granularity and SO65 MTF determination.

CONTENTS

Project Background

This report completes the postflight calibration of the Apollo 9 SO65 photography experiment. Earlier reports[1,2] described distortion, focal length, effective aperture, and resolution measurements on the four Hasselblad cameras used in the experiment. Also, an interim report[3] described the preliminary work on the investigation reported here.

The aim of this study was to obtain (1) a measure of the image degradation introduced by duplication of the original SO65 photography, (2) a comparison of the image quality in each of the three bands using black-and-white film. The established notation for these bands is BB (photar W58, green filter), CC (Photar 89B, ir filter), and DD (Photar W25, red filter), and (3) the operational MTFs for each band by comparison with simultaneous high-altitude (HA) photography.

The SO65 frame selected was number 3786, covering the desert northwest of Tucson, Arizona. Because the area is desert, the reflectivity in the green was very low, and the positive images from that band were dense. This is one example of a property unique to image evaluation of multispectral photography, i.e., the object(s) used for the evaluation are generally different in each band because of their spectral reflectivity properties.

The following sections outline the background for our approach to achieving these three goals, describe the measurement procedure, and explain in a consistent manner the results obtained.

Theory

The concept of linear transfer theory is well established in the literature.[4] In practice the objects used for evaluation of aerial photography by Fourier methods have been restricted to natural edges,[5] man-made edges,[6] man-made line sources,[7] and other, more sophisticated targets.[8,9] Most work has dealt with edge analyses primarily because they appear more frequently in some aerial scenes than other desirable targets or are the easiest to manufacture artificially. An extensive amount of literature has been published on techniques for edge analysis.[10-13]

The reason these basically simple targets have been employed is that we must know the spectrum of the object in order to apply linear transfer theory to the evaluation of an optical system. That is, in an equation of the form

$$I(f) = \tau(f)O(f)$$

where the image spectrum, $I(f)$ (assumed noiseless here), can be measured, the transfer function of the optics, $\tau(f)$, can be calculated only if the object spectrum, $O(f)$, is also known. In the case of an edge object, the edge is assumed to be of infinite extent in all directions, and the image is the edge spread function, or the integral of the line spread function

$$e(x',\theta) = \int_{-\infty}^{x'} l(x,\theta)dx$$

where θ is the azimuthal angle of the image. Now the spectrum of e cannot be found by direct Fourier transformation because the integral of e over all x is not finite.[14] Therefore, the derivative is taken

$$l(x,\theta) = \frac{d}{dx}\, e(x,\theta)$$

and then Fourier transformed

$$\tau(f_x,\theta) = \frac{1}{i2\pi f_x}\, F\left[\frac{d}{dx}e(x,\theta)\right] .$$

The transfer function obtained applies only to the direction x and in the area of the optical field where $e(x,\theta)$ was measured.

The above discussion was for a noiseless object and image. In aerial photography, grain noise in the film can be an important factor in image quality. Thus one consideration in ideal target selection should be signal-to-noise ratios throughout the passband of the system transfer function. One suitable definition of signal-to-noise ratio is the ratio of signal variance to noise variance at selected spatial frequencies. The contribution to the total variance of a function (the area under the squared spectrum) from each frequency interval is the spectral density integrated over that interval.[15] If $\phi_i(f)$ is the aerial image power spectrum and $\phi_n(f)$ is the film granularity power spectrum, we can say

$$\text{signal-to-noise ratio} = \beta(f) = \phi_i(f)/\phi_n(f)$$

where we have some leeway in defining n. Typically it is assumed that

$$s = i + n$$

or the noise is added to the aerial image thereby producing the total signal s.

In photography the noise spectrum is typically flat ("white") to high (on the order of 100 cycles/mm) frequencies. The signal-to-noise ratio then depends entirely on the shape of ϕ_i. The squared spectrum for an edge can be shown to be

$$\phi_i(\text{edge}) \approx 1/f^2 ,$$

and under the assumptions above

$$\beta(\text{edge}) \approx 1/f^2 .$$

Some work has been done on artificial targets having a β greater than that of the edge.[8]

Studies of typical aerial photographs[16] have shown that, excluding low frequencies,

$$\phi_i(\text{scene}) \approx 1/kf^2 .$$

Thus, depending on the value of k for the particular scene, as far as β is concerned, the edge target may have little advantage over a natural scene for image evaluation. Furthermore, the edge's unique direction and position in the image limit the analysis. Indeed, it should be realized that suitable edges do not appear in most aerial photographs, particularly in those for remote sensing of natural resources and similar studies.

Consequently, to evaluate the Apollo 9 imagery, we have used the natural terrain as the image evaluation vehicle and thereby gain some knowledge of typical image characteristics in the different spectral bands. We assume the terrain is typical of the set of possible scenes and that the photographic grain noise is random. We therefore make measurements in terms of "power" spectra, which in the photographic case are commonly called Wiener spectra. The MTF of the lens is then related to the image and object Wiener spectra by

$$|\tau(f)| = [\phi_i(f)/\phi_0(f)]^{1/2}.$$

Squared spectra are used because random noise destroys knowledge of the position of each image point; hence, exact spatial phase information is lost, particularly at higher spatial frequencies. Therefore, the complex OTF would contain spurious phase relations and be of little additional value over the MTF. Figure 1 shows how the phase is destroyed at higher frequencies. Useless values for the phase part of the OTF result at these frequencies.

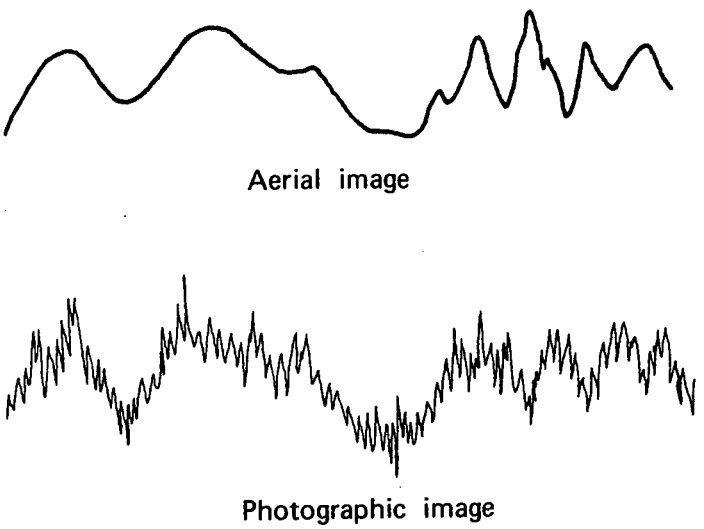

Fig. 1. Effect of grain in reducing spatial information.

It is important to keep in mind the implied linearity and stationarity of the transfer function approach. For a unique, noncoherent, optical system transfer function to be valid, measurements must be made in terms of intensities that are linearly related from object to image. In addition, the characteristics of the system, expressed either as a spread function or a transfer curve, must be stationary over the examined region of the image. Generally in photographic systems these criteria are not met for all ranges of exposure and all regions of the image. The familiar D-log E curve relating log exposure to resultant density gives only linear results in the transmission of the film for exposures within the straight-line region (if there is one) and for gammas of -1. Furthermore, development phenomena such as the adjacency effect depend in complicated ways on the contrast of the micro-image areas, conditions of development, etc., and consequently are nonlinear and nonstationary.

Further complications appear when we must examine image properties where grain noise is significant, i.e., at higher spatial frequencies. The noise is known to be dependent on the mean signal level both in density and transmission units. This simple fact destroys the stationarity of the aerial image, makes micro-image measurements difficult, and necessitates the use of estimation.

The D-log E nonlinearities can be removed by precise sensitometric calibration; adjacency effects can be accounted for with considerably more difficulty.[17] Techniques for treating signal-dependent noise have only recently been investigated.[18] In view of these restrictions on application of transfer theories, a more fruitful and useful approach may be to make measurements in terms of directly available quantities such as density or transmission, which indeed are the final output of the system, and to study pseudo-transfer functions that relate directly measurable input to output. However, these pseudo-transfer functions are input dependent and unique for the particular system (optics, film processing) considered.

In this work we have taken exactly this approach because of all the reasons above and also because of the lack of precise sensitometric information for the original data. Attempts have been made with some successes and some failures to remove some of the D-log E nonlinearities and to filter noise. We hope that the descriptions of the results in the following sections will give a clearer understanding of the phenomena involved and will also show the need for further work on problems such as nonstationarity and noise treatment.

Selection of Scanning Parameters

Laboratory measurements of three-bar resolution for the three black-and-white bands[2] indicated that the low-contrast operational photography would contain no image structure finer than about 30 cycles/mm. The transfer function of the microdensitometer, which is essentially determined by the slit spectrum at this low frequency, must have a sufficiently large value to measure the image modulation with reasonable accuracy at this frequency. Because the calculations are done in terms of spectra squared, the theoretical slit spectrum is

$$|\tau(f_x,f_y)_{\text{slit}}|^2 = \text{sinc}^2(af_x)\text{sinc}^2(bf_y).$$

In this equation a and f_x are the slit width and spatial frequency, respectively, in the scan direction, and b and f_y are the corresponding quantities perpendicular to the scan direction. The desired slit spectrum modulation transfer at 30 cycles/mm was chosen to be 0.5 so that

$$\text{sinc}^2(a30) = 0.25,$$

which gives

$$a \approx 0.020 \text{ mm}$$

for the slit width along the scan direction.

Now the width b perpendicular to the scan must be great enough that an essentially one-dimensional image spectrum is obtained and the grain noise is reduced to reasonable values. Because of the limited instrument magnifications and the scale change necessary to measure the HA photography explained below, the maximum possible length of the slit was about

$$b \approx 4.5 \times a = 0.090 \text{ mm}.$$

To effectively compare the SO65 and HA images, the same ground area must be scanned in both cases. This necessitates scaling the measuring slit. From measurements between identical ground points in the two sets of photographs, we found the scale factor to be approximately 11. The slit dimensions for the HA scan were then nominally 0.220 mm for a and 0.990 mm for b. The length b was the maximum allowed by the available optical magnifications and preslit iris size. Thus combined with the scale factor of 11, it limited the length of the slit for the SO65 measurements to 0.09 mm as mentioned above.

The two concepts of sampling and aliasing determine the sample interval for given data. According to the sampling theorem for band-limited functions such as the optical image, the sample interval must be[19]

$$\Delta x \leqslant 1/2f_c$$

for $f_c \approx 30$ cycles/mm, $\Delta x \leqslant 0.017$ mm. However, we must measure a noisy image where the grain spectrum may extend to 100 cycles/mm.[20] A problem unique to equispaced analysis now arises, i.e., aliasing. If the sampling rate is such that $1/\Delta x < 2f_n$, where f_n is the noise cutoff frequency, spurious values of the spectrum will result because the replicated spectra (see Appendix B) may overlap considerably. The calculated spectrum will contain power at some frequencies concealed ("aliased") as power at other frequencies (Fig. 2). To avoid aliasing, Δx must be sufficiently small to include these spectra within the folding or Nyquist frequency. Thus we selected the value $\Delta x \approx 0.005$ mm so that the Nyquist frequency would be $f_N = 1/2\Delta x \approx 100$ cycles/mm. The actual errors experienced with aliasing grain spectra have not been reported. Because the slit spectrum acts as a filter to reduce the modulation at higher frequencies (by a factor of about 10^{-4} in the squared spectrum between 30 cycles/mm and 100 cycles/mm) the Δx chosen above should be sufficiently small.

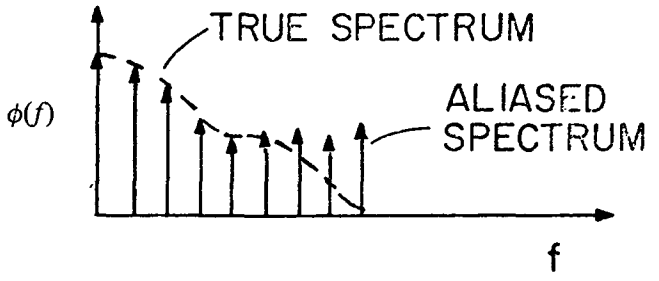

Fig. 2. Photographic image spectrum.

In the case of the HA evaluation, the sample interval cannot be scaled merely by the factor of 11 because the grain spectrum is as wide as that in the SO65 image. Because the slit spectrum in this case falls off very rapidly, going to the first zero at about 5 cycles/mm, and to reduce the amount of data taken, a factor of 2 was allowed in the sample interval, giving $\Delta x \approx 0.010$ mm and $f_N \approx 50$ cycles/mm.

Selection of Optics

The image scans were made with a Joyce-Loebl MK III CS microdensitometer. The basic optical train is shown in Fig. 3. In operation, the preslit illuminates an area of the film, which is imaged by the efflux optics onto a postslit. The postslit generally defines the area to be sampled in the image.

It has been shown, theoretically[21] and experimentally,[22] that for a microdensitometer to operate in a noncoherent mode, i.e., the measured irradiance passing through the postslit is directly proportional to the intensity transmission of the sample, the ratio of numerical apertures (NA) of influx to efflux optics must be

$$\mathrm{NA}_{\text{influx}}/\mathrm{NA}_{\text{efflux}} = \epsilon > 1 + \eta_0/\sigma_0$$

where η_0 is the highest spatial frequency of interest in the sample and σ_0 is the "cutoff frequency" of the efflux optics. We see that the efflux optics must be overfilled by the influx optics to retain noncoherence up to η_0 cycles/mm. For this study we chose a 5X, 0.1 NA objective and a 5X, 0.2 NA condenser. For $\eta_0 = 30$ cycles/mm, and $\lambda \approx 5 \times 10^{-4}$ mm, $\epsilon = 2 > 1 + 0.08$, and the condition for noncoherence is satisfied. The operating NAs of the objective and condenser were not the same as those specified above because the lenses were not used at the specified magnifications, however, the ratio of NAs is essentially the same.

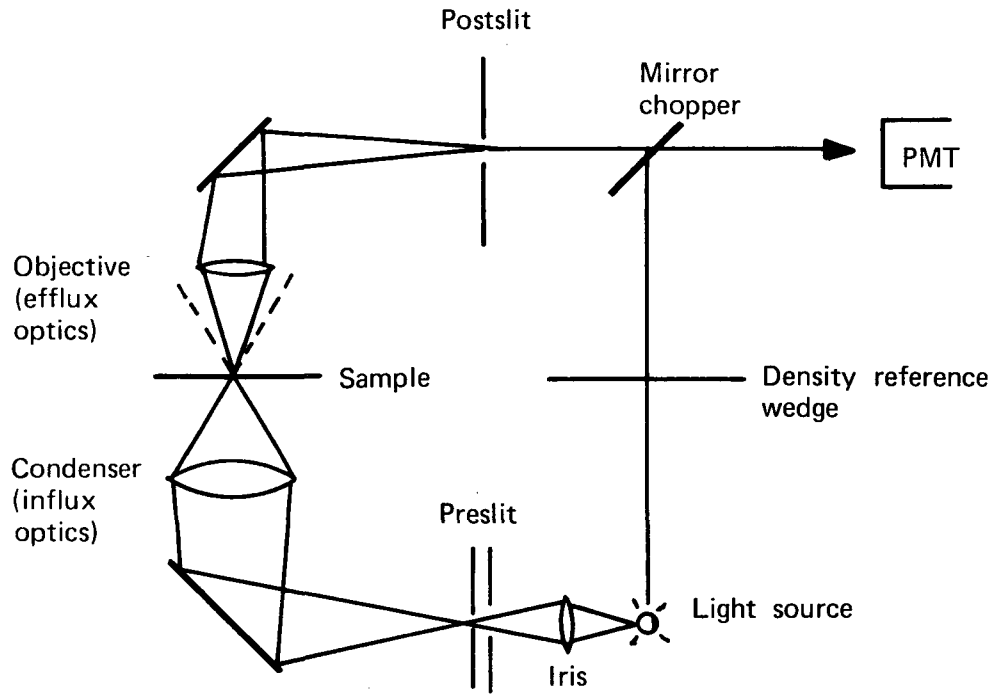

Fig. 3. Joyce-Loebl MK III CS optical schematic.

Calibration of the Instrument

The Joyce-Loebl microdensitometer measures optical density, $D \equiv -\log T$, linearly by comparison of the sample beam and a reference beam that passes through a calibrated density wedge. This arrangement makes the instrument almost independent of time-varying effects such as temperature changes. Thus photometric calibration is relatively easy and can be performed by placing neutral density filters anywhere within the sample beam. For our data, a reference range of 0 to 1.6 density units was chosen to provide maximum density resolution in the digital values, which were fixed at a maximum number of 168 possible numbers. We therefore obtained a density resolution of about 0.01 density units. The voltage signal out of the instrument was generally zeroed with no sample in the beam. When necessary the zero was set at a known density (0.3, 0.5, or 1.0) to extend the upper range of the instrument for higher density samples. Calibration with neutral density filters as mentioned above showed the output to be linear and accurate up to densities of about 1.8. All the imagery had densities below this value.

The microdensitometer uses a direct mechanical link between sample and recorder stages. The ratio of the lever arms of the link provides a variable scale change between the two stages. The recorder stage is connected to an encoder that electronically samples the scan in points/unit distance. Nominal values of 50:1 for the ratio arm and 100 points/inch sample rate (at the recorder stage) were selected to give a basic sample interval at the film of 0.005 mm. The sample rate could be varied by multiples of two for larger sample intervals. Calibration was performed by scanning a resolution target bar of known width, converting the density values obtained to transmittances (to linearize the convolution slope at each edge of

the bar), and counting the sample intervals between 50% transmission points. The basic sample interval was found to be $\Delta x = 0.0059$ mm, and the steps of 2 were accurate multiples of this figure. Consistency of this interval during the scan was not measured but appeared to be good because the same number of points was obtained for all scans.

Because the sample moved continuously during the scan, a time convolution was performed on the image in addition to the familiar slit convolution. The time convolution was converted to a spatial operation by multiplication with the time interval during the sampling process. Thus it appeared as part of the MTF of the microdensitometer and was included in that calibration. The scanning speed was adjusted to accommodate the response time of the instrument and the associated digitizing electronics. The feature of the Joyce-Loebl microdensitometer that varied the speed of the scan with the rate of change in sample density was disconnected during the measurements to provide a more consistent scan speed.

The film samples were sandwiched between two thin glass plates to maintain flatness over the scan region. The plate on the objective side of the film introduced some spherical aberration into the image formed on the postslit. However, this effect was part of the over-all microdensitometer MTF and cancelled in the ratios of second and fourth generation spectra. In any case the aberration was small. The amount of third-order wavefront aberration introduced is given by

$$W_{SA3} = -1/8\left\{[(\mu^2-1)/\mu^3](\mathrm{NA})^4 t\right\},$$

where t (thickness of plate) = 1.2 mm, μ (index of glass/index of air) = 1.5, and NA = 0.1. For $\lambda = 5.5 \times 10^{-4}$ mm, $W_{SA3} = -0.01$ waves.

The depth of focus is also important in microdensitometry. According to the Rayleigh quarter-wave criterion, the depth of focus in object space is

$$\delta f \approx \pm \lambda n'/2(\mathrm{NA})^2.$$

For our case NA = 0.1, $\lambda \approx 5.5 \times 10^{-4}$ mm, n' (index of film and glass plate) ≈ 1.5, and

$$\delta f = \pm 4.2 \times 10^{-2} \text{ mm}$$

$$= \pm 42\ \mu\text{m},$$

which is much greater than the emulsion thickness of the samples. In practice, it was not difficult to maintain focus throughout a scan.

Data Measurement

The image area scanned is shown in the HA photograph on the following page. This area was scanned in the second and fourth generation SO65 copies (both positives of the object scene) for the three black-and-white bands (basically covering the red, green, and near-ir

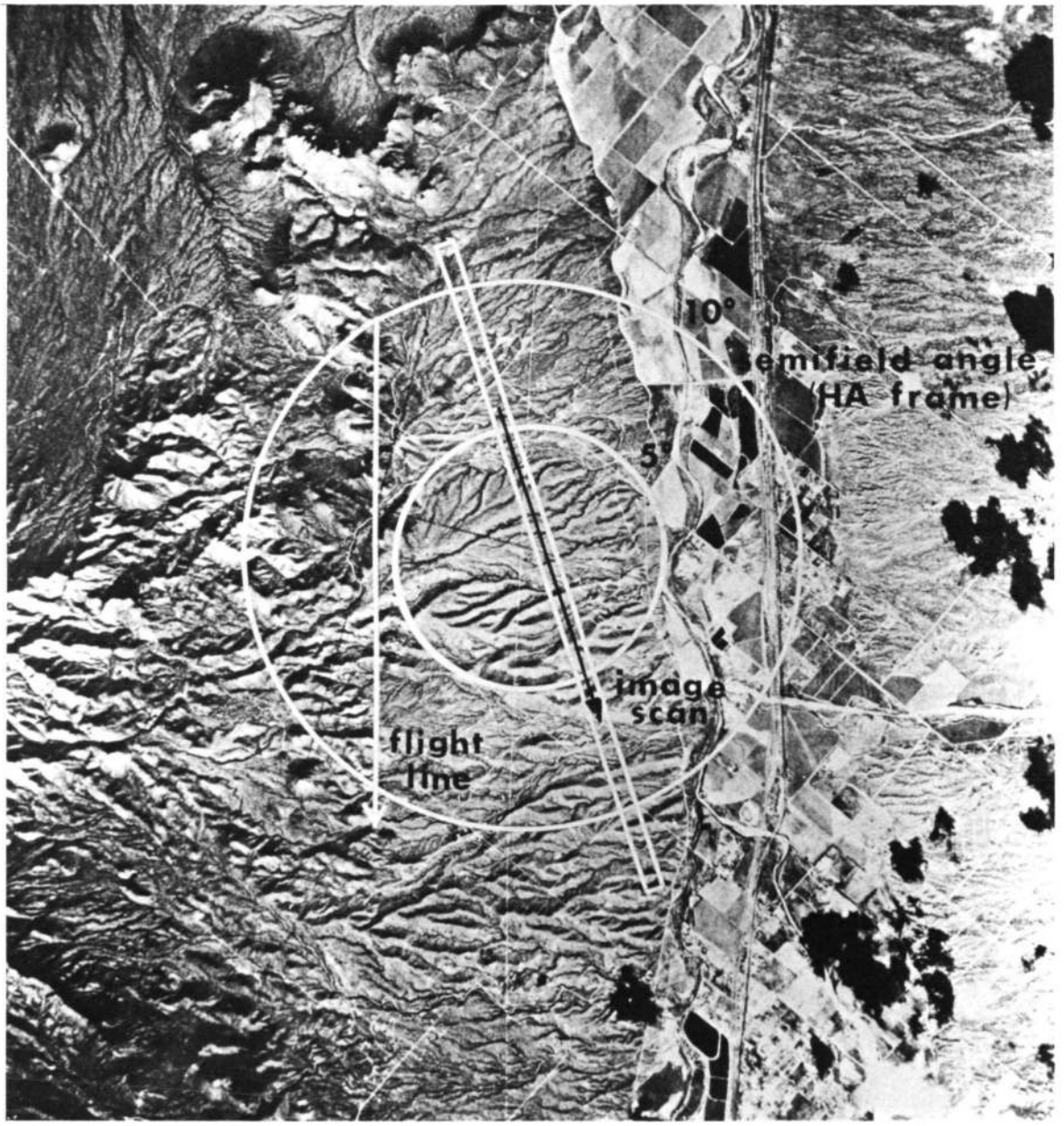

High-altitude photograph of the image area that was scanned.

spectral regions) and also in the three bands of HA imagery available. In addition, scans were made of the step tablets added to the duplicates (see Fig. 4) and of the step tablets attached to the HA film. The quantity of data required became rather large, roughly

$$\begin{aligned}\text{SO65 data points} &= 3 \text{ bands} \times 2 \text{ duplicates} \times 1000 \text{ pts/scan} \\ &\quad + 3 \text{ bands} \times 4 \text{ step tablets} \times 7 \text{ steps} \\ &\quad \times 1000 \text{ pts/scan} \\ &= 90{,}000 \text{ pts}\end{aligned}$$

$$\begin{aligned}\text{HA data points} &= 3 \text{ bands} \times 1000 \text{ pts/scan} \times 5 \text{ scans} \\ &\quad \text{(to cover same ground area)} \\ &\quad + 3 \text{ bands} \times 1 \text{ step tablet} \times 7 \text{ steps} \\ &\quad \times 1000 \text{ pts/scan} \\ &= 36{,}000 \text{ pts}\end{aligned}$$

for a total of 126,000 data points. Naturally computer processing was necessary, but the sheer bulk of the data created some difficulty in handling.

To provide good sensitometry, a sensitometric strip was added to both ends of the film before each duplication. The $DATA_1$ strip contained a step tablet (on film of the same type as the flight film and exposed with a daylight source modified by the appropriate filter for each band) and a straight edge of known quality that was contact printed onto the strip. The $DATA_2$ and $DATA_3$ strips were on the duplicating film, Kodak Aerographic duplicating film, type 2420. Each final duplicate appeared as shown in Fig. 4. The edge was included to provide calibration of the microdensitometer and verification of results from the image scans, but spots on the edge exposures prevented their use.

We should note that the step tablets scanned in the SO65 photography were the $DATA_1$ strips and not the original SO65 friskets calibrated by Data Corporation. Thus, the granularity values obtained may not correspond exactly with those in the images but should at least be representative and describe the duplication accurately. In the following section we can see that the granularity measurements from these data agreed closely with published data from Kodak.

In the rest of this report the first copy (a positive of the aerial scene) of the original film will be referred to as the second generation duplicate, the copy of that as the third generation, and the final duplicate, also a positive of the aerial scene, as the fourth generation.

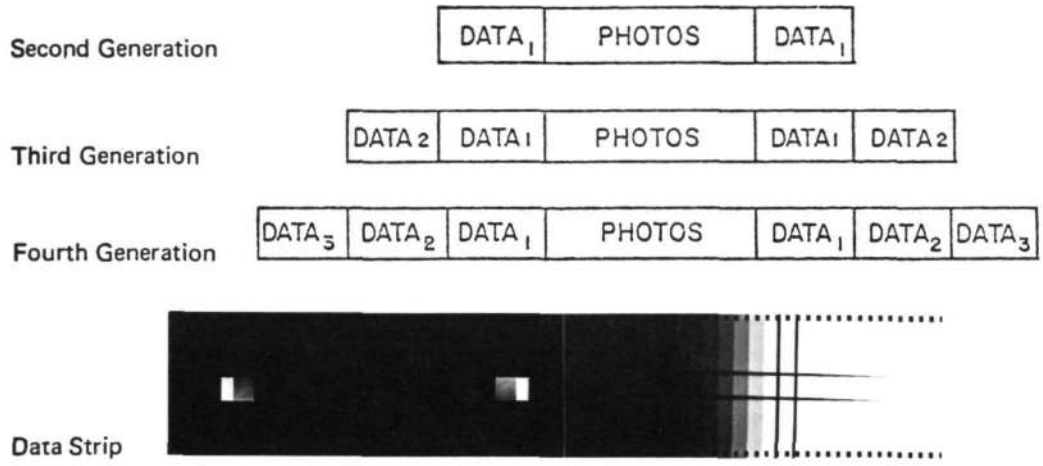

Fig. 4. Special sensitometry for SO65 duplication.

Granularity Analysis

The first step of the analysis was calculation of the statistical properties of the step tablet scans. The standard deviation in density readings for each step is plotted as a function of the mean specular density ($\overline{D}$) of that step in Figs. 5 through 7. As a check of the numerical results, we note that the granularity of film is defined by Kodak[23] to be $G = 1000\,\sigma_D$. The mean density is 1, the scanning aperture is 0.048 mm diam, and the area A_K is 0.0018 mm^2. For Pan-X 3400 film the granularity is 20, and for ir aerographic 5424 the granularity is 38.

It is well known that the granularity depends on the inverse square root of the scanning aperture area. In our measurements, the area was approximately 0.020 X 0.090 mm^2 or 0.0018 mm^2, i.e., the same as A_K. From Figs. 5 through 7 for the original film, our measurements showed that the granularity for the Pan-X 3400 film was 25, and for the ir aerographic film 5424 it was 45.

Normalizing these values by the square root of the aperture area ratio leaves them unchanged, for

$$(A/A_K)^{1/2} = 1.0.$$

The differences between our values and those of Kodak could be due to development variations or measurement differences (circular spot or slit). However, the values are within 25% and considered good.

The most significant fact apparent in Figs. 5 through 7 is the increase in granularity for each successive duplication, at least for densities less than 1.5. The reduction of granularity at higher densities is probably a saturation effect due to close packing of the grains and has been included in recent theories.[24] It is obvious that, even if the MTF of the duplication

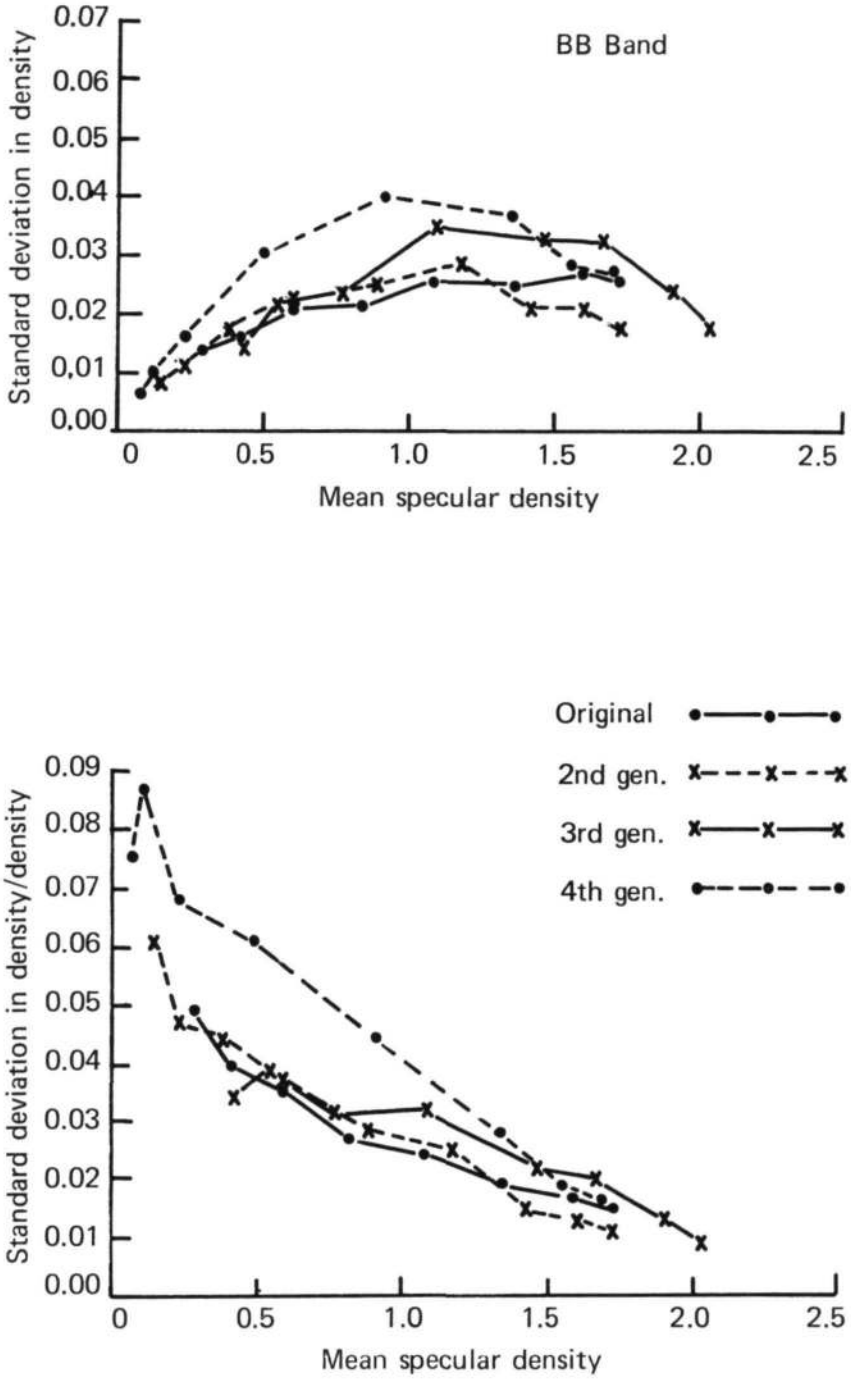

Fig. 5. (top) Standard deviation in density as a function of mean specular density for BB band. (bottom) Average error in a single measurement of density as a function of mean specular density.

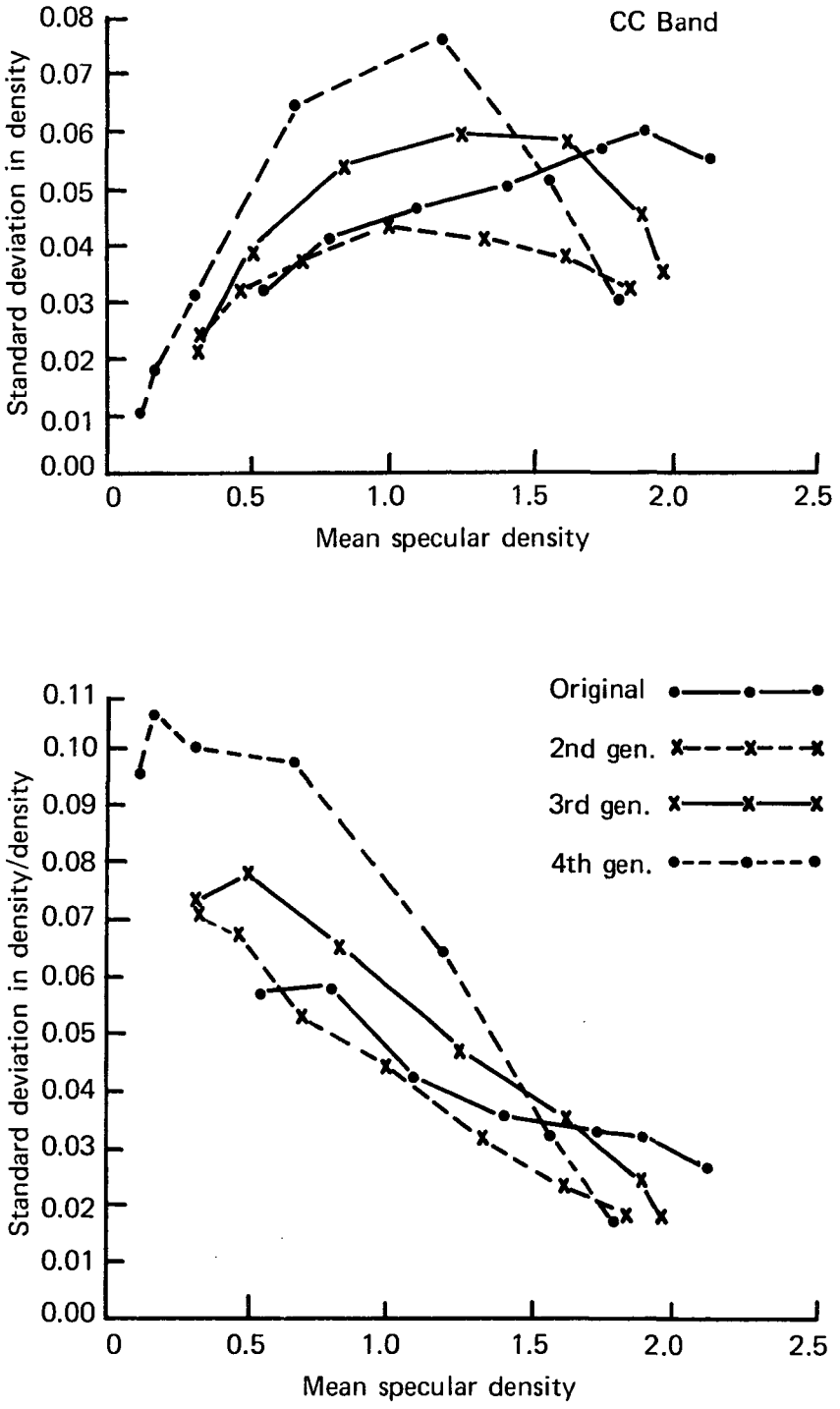

Fig. 6. (top) Standard deviation in density as a function of mean specular density for CC band. (bottom) Average error in a single measurement of density as a function of mean specular density.

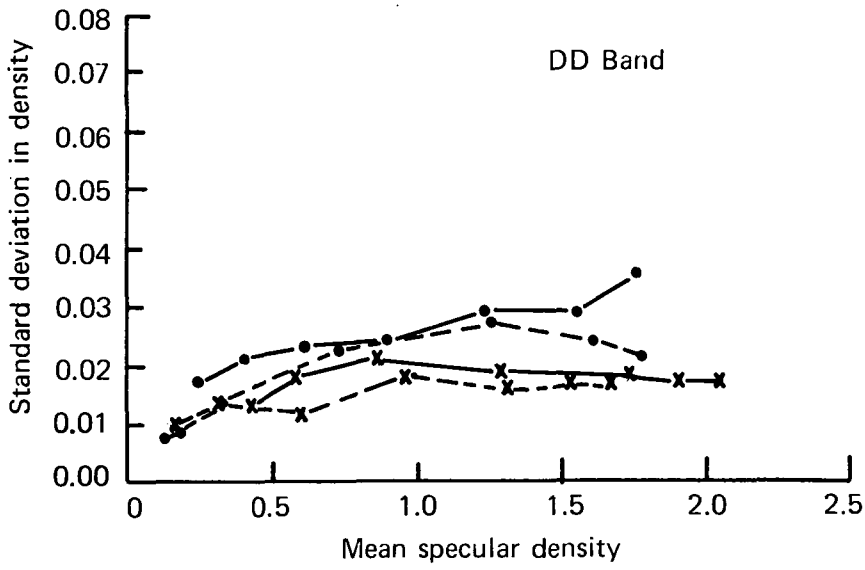

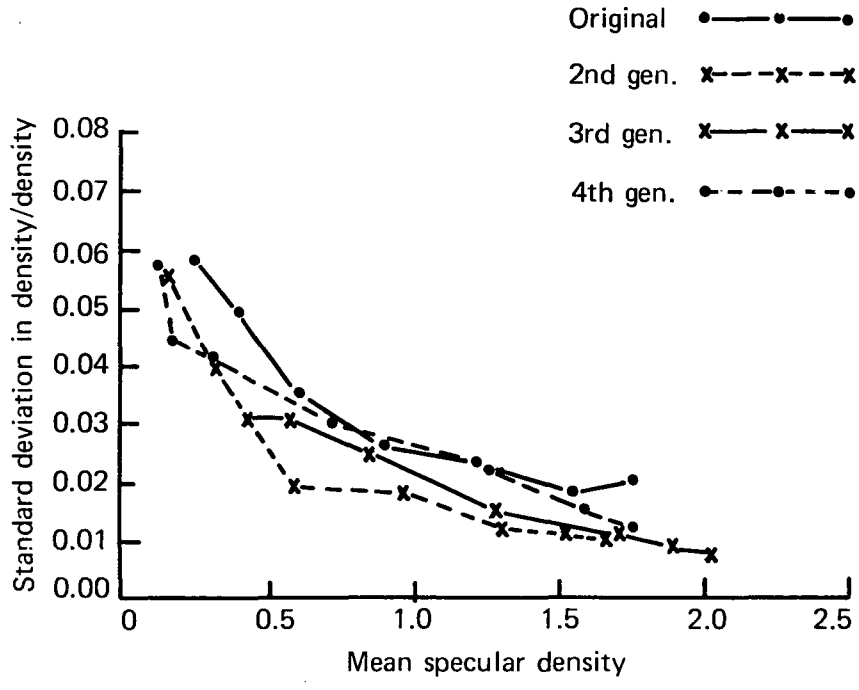

Fig. 7. (top) Standard deviation in density as a function of mean specular density for DD band. (bottom) Average error in a single measurement of density as a function of mean specular density.

process,(i.e., the product of the positive film MTF and the printer MTF)is 1, the copy is going to be more grainy and therefore suffer degradation. Jones and Trinks[25] concluded the same result for a case where the MTF of duplication was greater than 1 at all frequencies.

Furthermore, we note that the *increase* in granularity depends on the granularity of the original, as evidenced by comparison of the BB and DD bands with the CC band. Indeed, *at a density of 1.0*, the percentage increase in σ from second to fourth generation is

$$\begin{aligned} \text{BB:} \quad & \Delta\sigma_{24} = +54\% \\ \text{CC:} \quad & \Delta\sigma_{24} = +67\% \\ \text{DD:} \quad & \Delta\sigma_{24} = +39\% \end{aligned}$$

The other sets of curves in Figs. 5 through 7 represent the average error due to granularity in a single measurement of density. This quantity is interesting because it is a measure of the uncertainty in estimating the aerial image intensity from the grainy recorded image. In general, the error is greatest for low densities and decreases at higher densities, again because the grains become closer and closer together, giving a more uniform density. Also we can see that it increases from copy to copy, meaning a single measurement at a given density is less reliable in the fourth generation than in the second generation. The effect of this error on the calculated image spectra has not been determined for this work, but it is worth investigating. In edge gradient analysis the error is reduced by averaging several traces across the edge at different places. However, in the method used here, we need to either filter the noise or use the computer to generate many sets of new data points, which are distributed about the measured data according to the probability distributions of densities from step tablet scans. Each set of artificially generated data would then be Fourier transformed and the spectra averaged over all sets to obtain a final smooth spectrum estimate.

Finally the curves of σ versus $\bar{D}$ show the obvious dependence of the noise σ on the mean signal level $\bar{D}$. If the noise were independent of $\bar{D}$, these curves would just be straight lines parallel to the abscissa.

Duplication was done by contact printing with a Kodak Niagara printer. The unexposed film was sandwiched to the original, emulsion to emulsion, and exposed through the original by a mercury arc lamp. The lamp was about 8 in. from the film, and the exposure area was determined by a 2-in. aperture over the moving film. Therefore, the incident light was reasonably normal to the film during exposure.

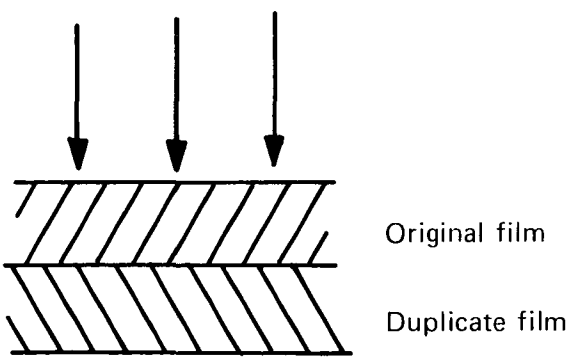

The duplicate film integrated over 2π steradians all the light transmitted by the original. Therefore, the proper quantity to consider in duplication was the totally diffuse density or transmission.[26] Conversion of the specular densities as measured by the microdensitometer was accomplished by dividing by the Callier Q factor. To determine Q, all the step tablets were measured on a MacBeth TD-102 densitometer with a 1-mm aperture. The mean of the specular densities for each step was calculated, to give an effective large-area measurement, and divided by the diffuse density to determine Q. The values of Q are plotted in Fig. 8 as a function of specular density for the second and fourth generation duplicates. In the density regions of interest, Q is essentially constant, but a linear interpolation method was used to convert specular to diffuse densities on the computer.

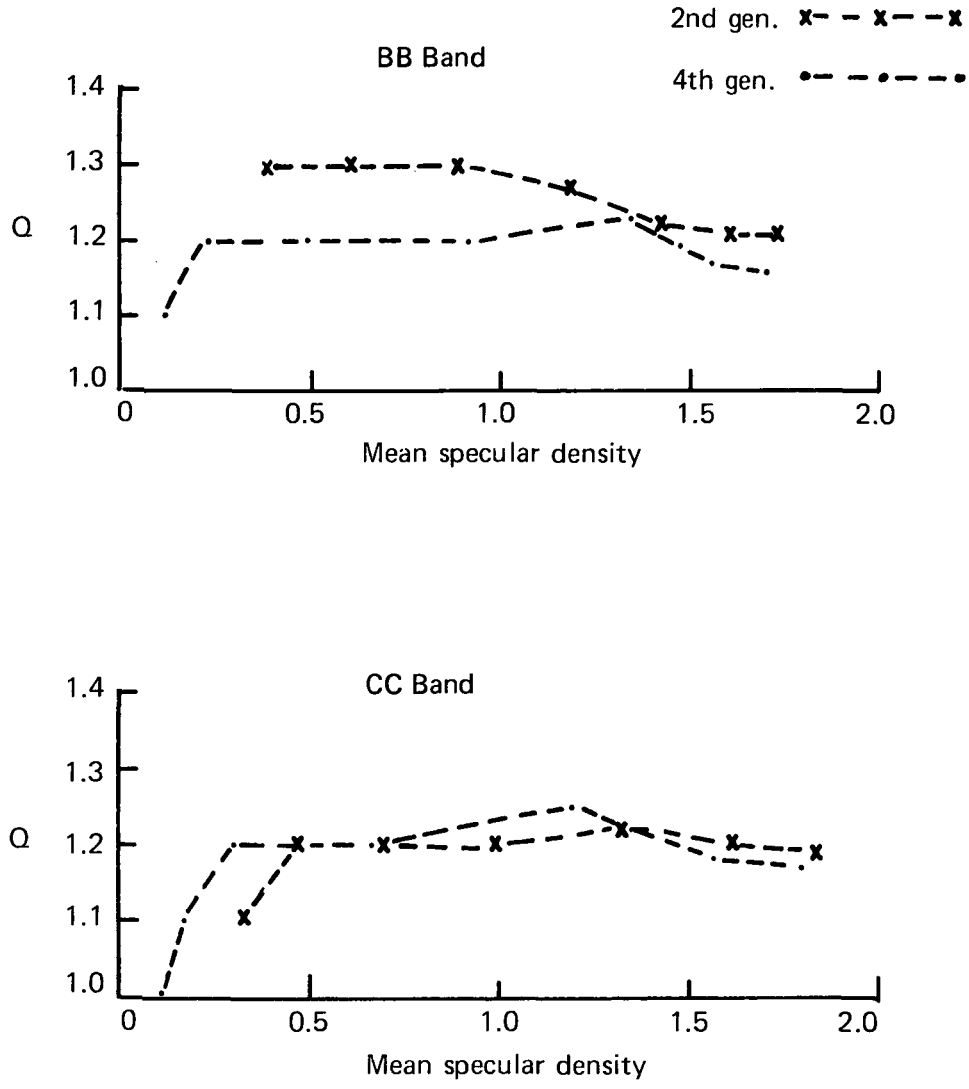

Fig. 8. Callier Q factor as a function of specular density.

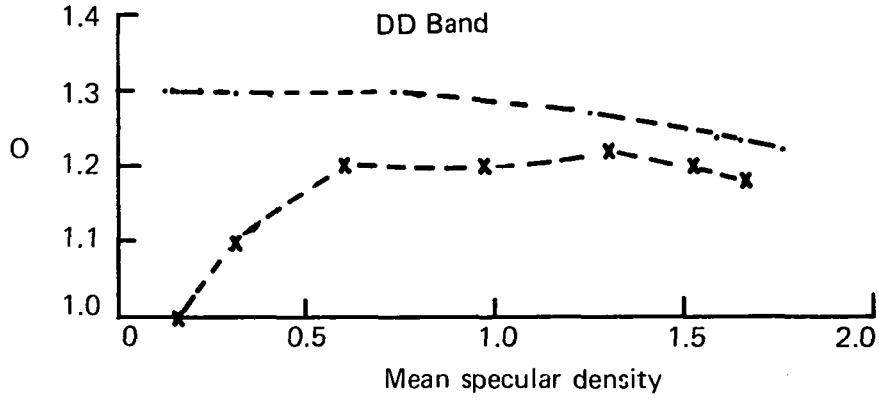

Fig. 8. (Continued).

Diffuse densities were then converted to diffuse transmission values by the logarithmic definition. Because of the nonlinear relationship between T and D as shown in Fig. 9, values of σ_D for higher values of D correspond to smaller values σ_T, but the ratio $\sigma_T/\overline{T}$ becomes large. Thus the relative error in single measurements of T is greater than that in D for higher densities.

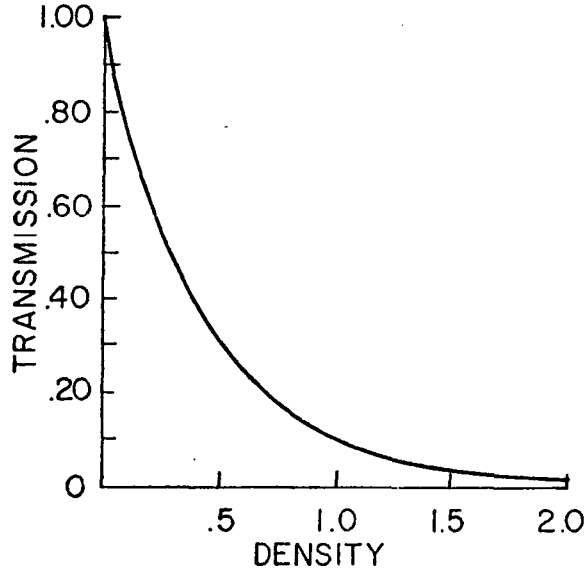

Fig. 9. Nonlinear relationship between T and D.

Sensitometric Analysis

By plotting the mean densities of a step tablet from one generation versus the mean densities of the same steps in the previous generation, we obtain an effective D-log E curve. Note that the exposure of the copy is

$$E' \approx T_0 = 10^{-D_0}$$

$$\log E' \approx -D_0 .$$

Therefore, compared to the familiar form, the curves are reversed in sign along the abscissa. Figures 10 through 12 show such curves for each duplication step and an over-all D-log E curve from second to fourth generation. Each graph shows the diffuse density curve and the specular density curve, along with the mean density level in the image of that particular generation. The diffuse density gammas (slopes) were calculated *at these image densities* by differentiating a third-order polynomial fit to the curve. The results are

	Gamma (at image density)		
Duplication	**BB**	**CC**	**DD**
4/3	-1.51	-1.35	-1.19
3/2	-0.91	-1.14	-1.26
2/0	-1.26	-1.20	-1.23
4/2*	+1.42	+1.49	+1.47

*Over-all

The over-all γ for second to fourth generation was about 1.45 for all cases, but the BB band shows the most fluctuation in the γ of each duplication. It is interesting to note that the product of the γ for 4/3 and 3/2 agrees very closely in all bands with the over-all γ for 4/2, i.e,

$$\gamma_{42} \approx \gamma_{43}\gamma_{32}.$$

Image Scan Analysis

Sections of the image scans from each second generation band are shown in Fig. 13. Note that (1) the BB band is the most dense, partly owing to the low reflectivity of the desert in the green and insufficient exposure of the original, (2) the CC band has more noise at higher frequencies than the other two, and (3) the DD band possesses the highest image modulation. These observations are reinforced by the behavior of the spectra shown later.

The Wiener spectra of these traces were calculated in both density and transmission units. The mean was subtracted from the data before Fourier transformation to eliminate sharp steps at the ends of the data. In all cases 512 data points were transformed, resulting in 256 unique values (because the spectrum is even) of the spectrum modulus at the sampled

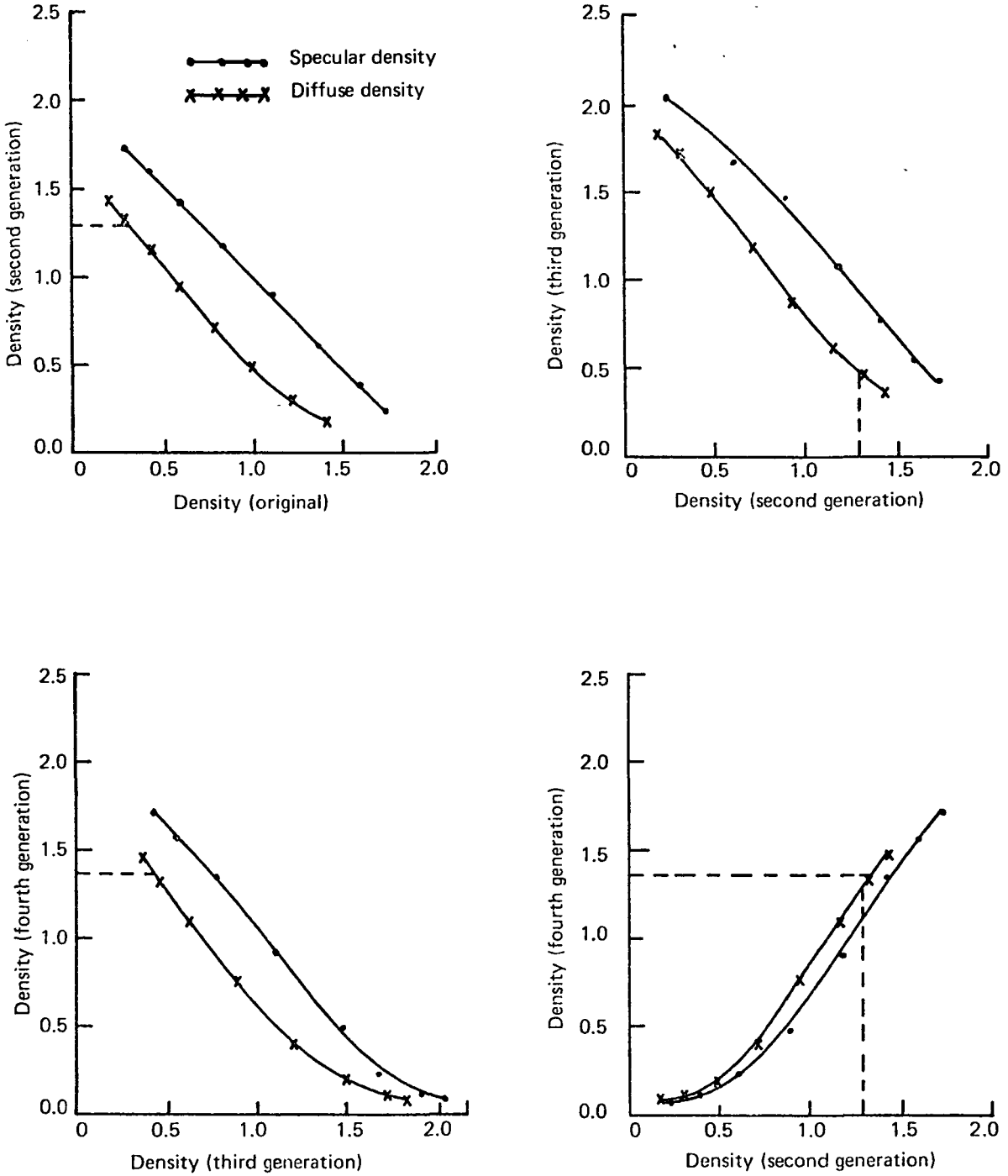

Fig. 10. D-log E curves for BB band.

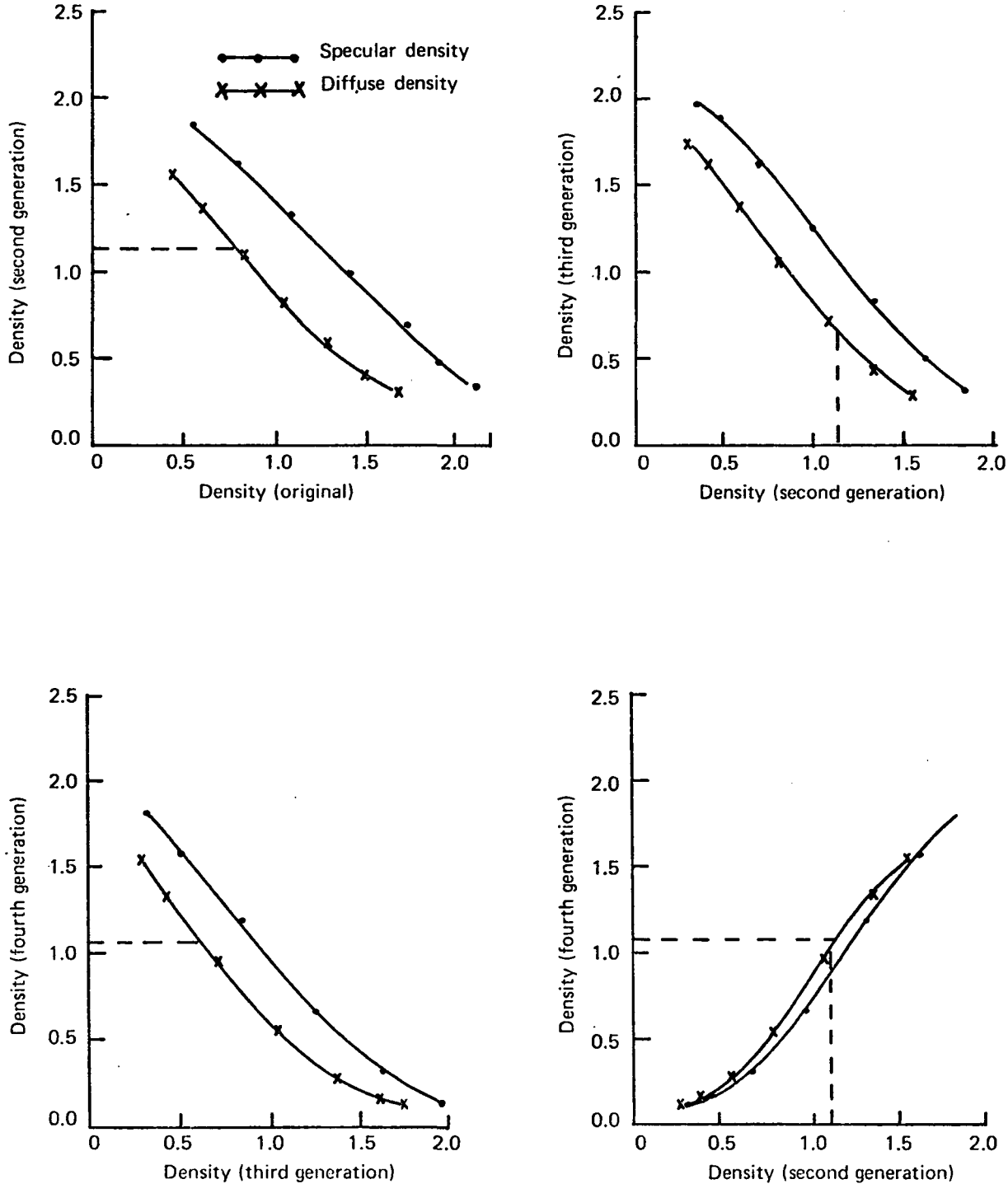

Fig. 11. D-log E curves for CC band.

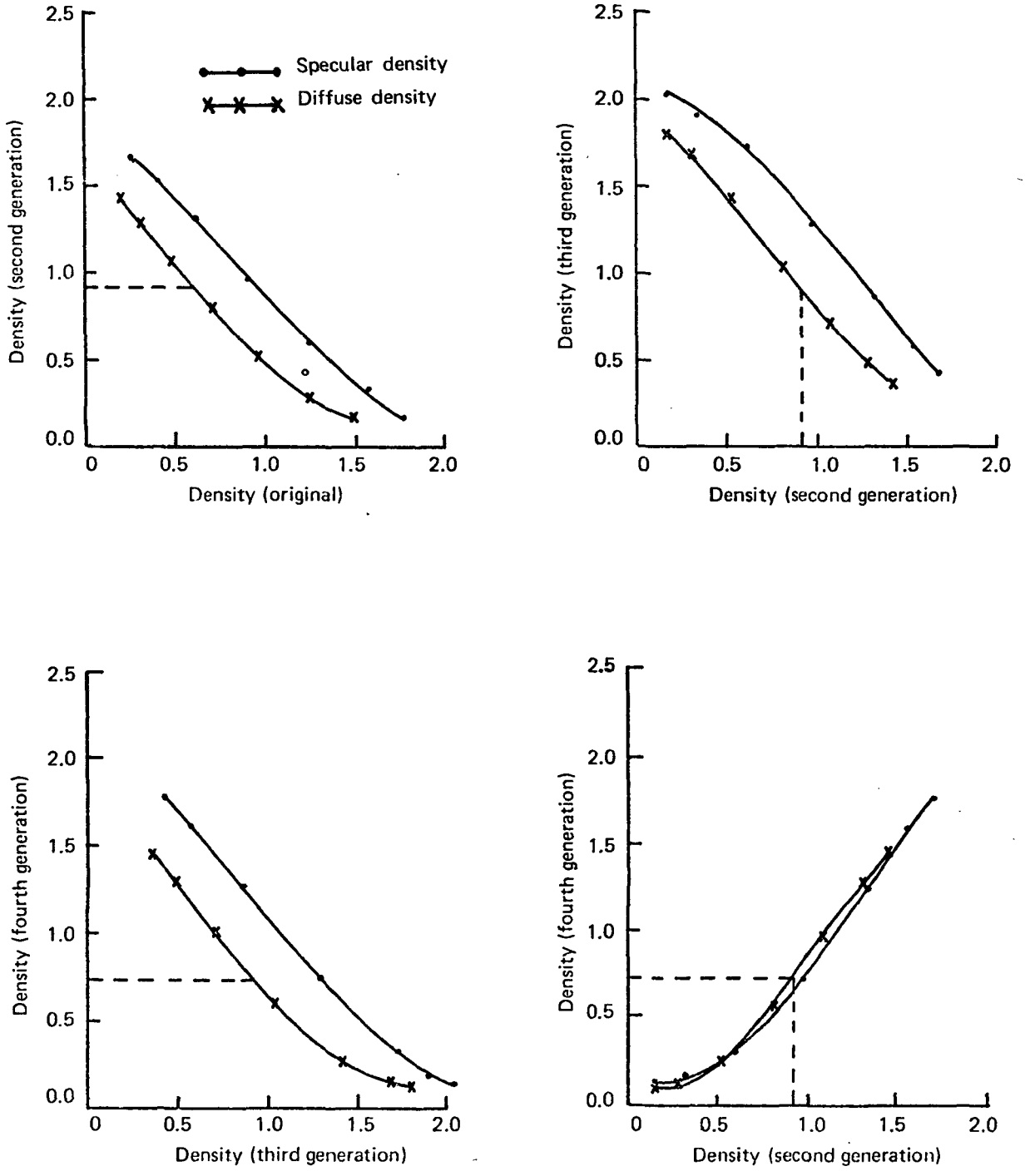

Fig. 12. D-log E curves for DD band.

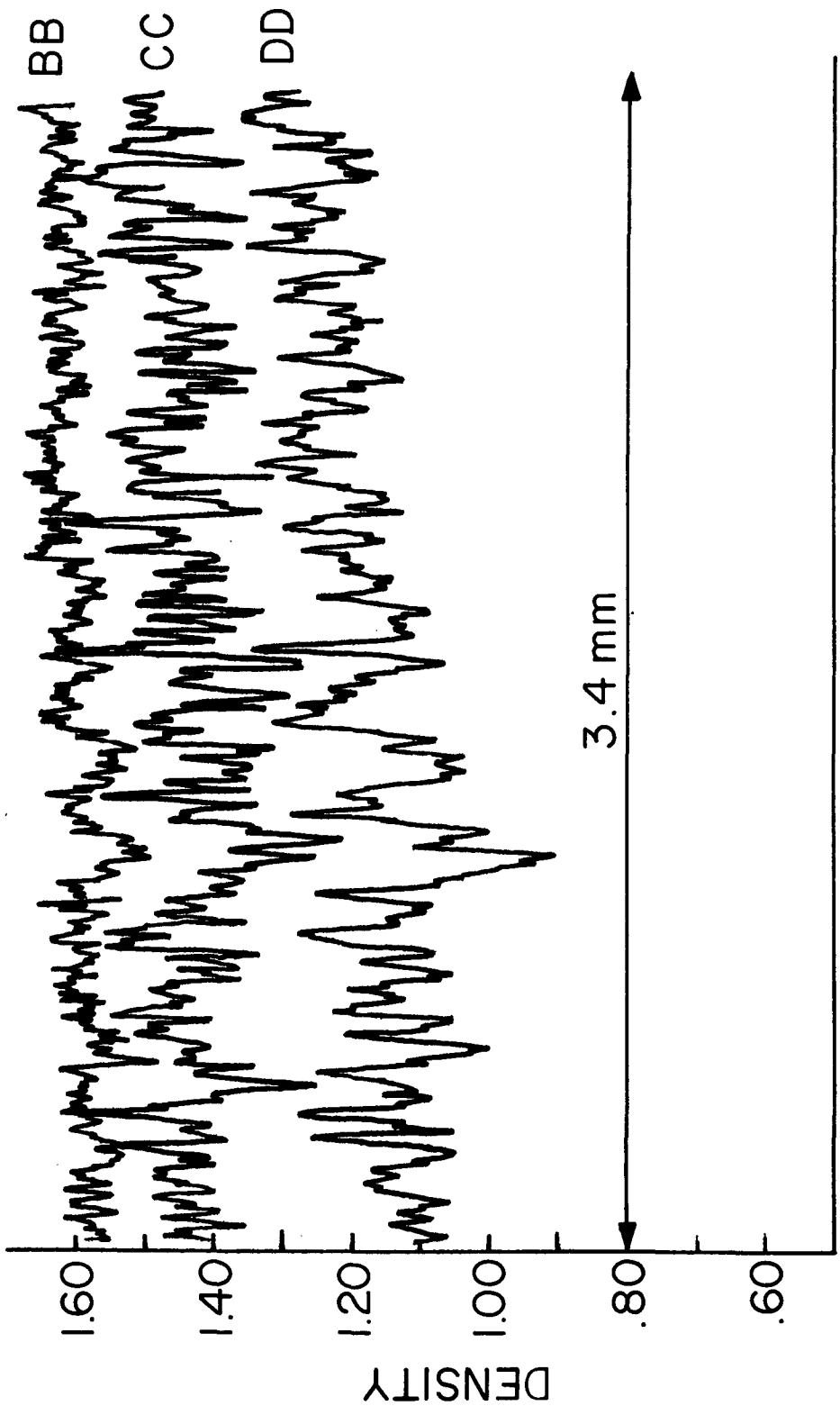

Fig. 13. Image scans, second generation.

frequencies spaced $1/N\Delta x$ cycles/mm apart. For our case

$$1/N\Delta x = 1/(512 \times 0.0059) = 0.33 \text{ cycles/mm.}$$

These values were integrated over 2 cycles/mm bandwidths throughout the spectrum as shown in Fig. 14. The spectra used in MTF calculations were these average values in 2 cycles/mm intervals and hence were smoothed to that extent. This may not at all be an optimum smoothing interval, which may even vary across the spectrum, but time was insufficient to investigate other possibilities.

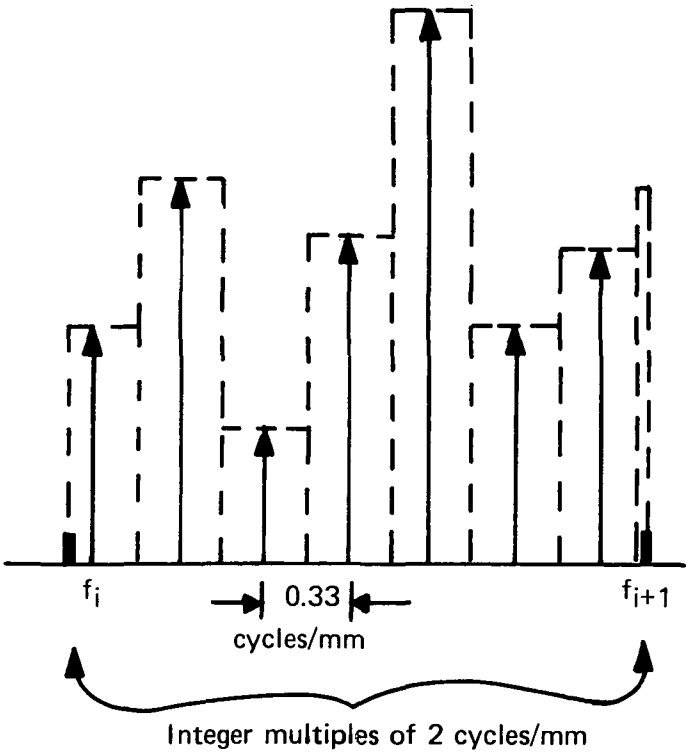

Fig. 14. Integration of spectrum values.

Spectra of the second generation images, *including* the filtering of the scanning slit, are shown in Fig. 15. The spectra have been normalized at low frequencies, but the area (total variance) differs in each band. Several comments can be made immediately.

(1) The spectra fall off rapidly as spatial frequency increases.

(2) The BB band has the least image structure as evidenced by its more rapid decrease in spectral power.

(3) The CC band has the largest amount of grain noise.

(4) The DD band appears to be the strongest in image modulation below 8 cycles/mm.

(5) The diffuse density and diffuse transmission spectra are the same within 0.05. This can be explained by the low contrast of the images, which nullifies the nonlinear logarithmic D-T relation. However, the absolute areas under the spectra, representing the total variance, are vastly different.

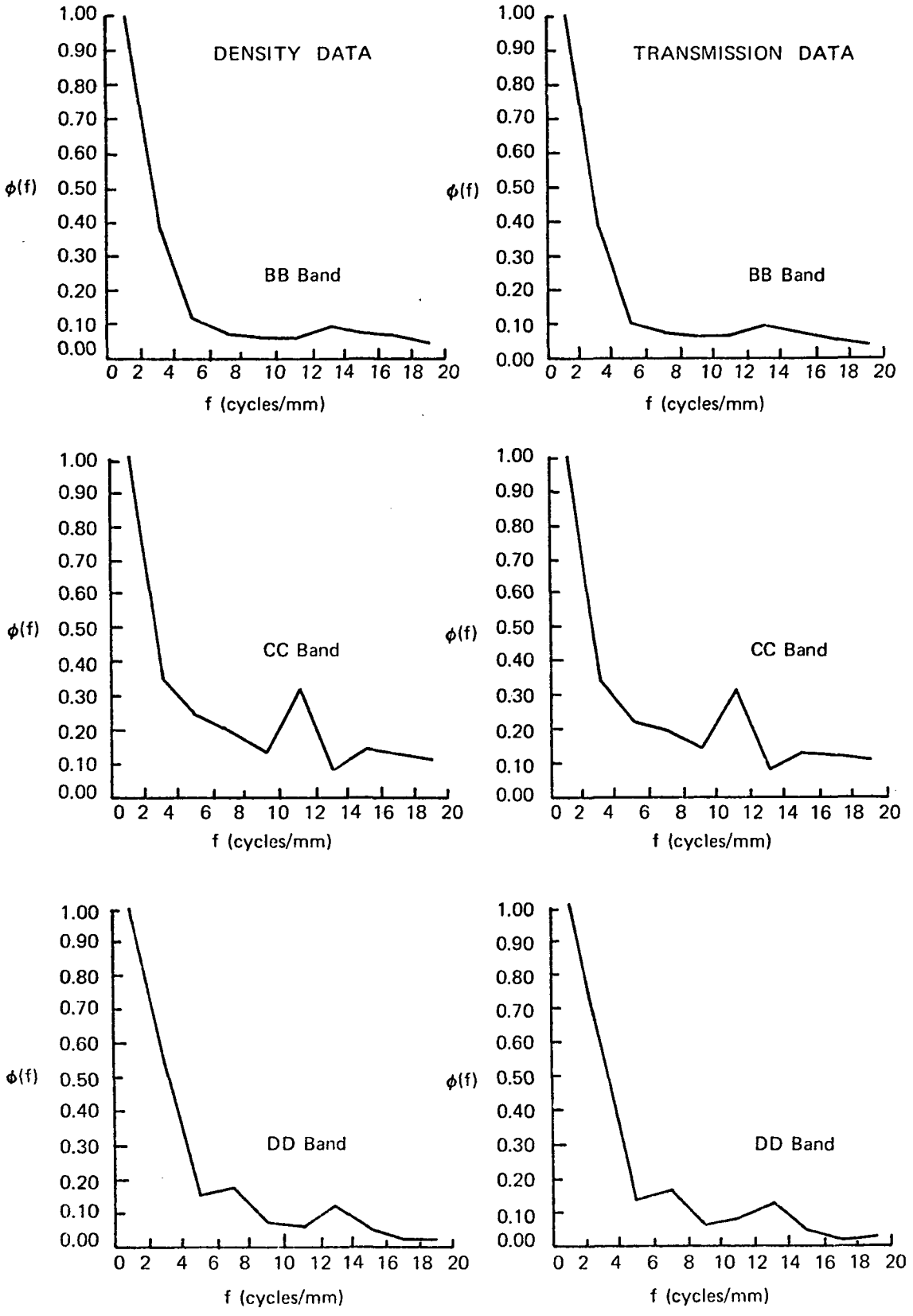

Fig. 15. Second generation image spectra.

Comparison of Image Quality in Each Band

The signal-to-noise ratio was calculated for each band using the definition

$$\text{signal-to-noise ratio} = \beta(f) = \phi_i(f)/\phi_n(f) = \phi_s(f)/\phi_n(f) - 1.$$

Noise data were obtained from the step tablet scans by selecting the step whose mean transmission was closest to that of the image. The mean (and hence the standard deviation) for the noise was then linearly interpolated from Figs. 5 through 7 to correspond to the exact mean of the image. The spectrum of the selected step was then scaled by the interpolated variance. The values of β are absolute in the sense that the slit transfer factor cancels out in the ratio.

Plots of $\beta(f)$ for the second and fourth generations of the three bands and for two sections, I and II, of the image are shown in Fig. 16. The strength of the image in the red (DD) band compared to the other two is immediately apparent. The BB band has the lowest signal-to-noise ratio, less than 5, for all frequencies. However, above 5 cycles/mm the BB and CC bands are equally poor with β being on the order of 1 or less.

In the fourth generation β increases for some frequencies and decreases for others. The increase in β is particularly noticeable at higher frequencies, probably owing to nonlinear enhancement of the image as discussed in the following section.

Comparison of Image Quality in Second and Fourth Generations

The transfer factor for duplication was calculated by the ratio

$$|\tau_{dup}(f)| = [\phi_4(f)/\phi_2(f)]^{1/2}.$$

Several overlapping data sections of 512 points each were taken from the scans, a transfer factor was calculated for each, and the average $|\tau|$ was calculated. The transfer function of the slit and microdensitometer cancels in this ratio. Keeping in mind the discussion of linearity in the section on theory, we can see that $|\tau|$ will be somewhat object dependent and that values obtained from each data section above will not be the same. Nonstationary grain noise will also cause variation in $|\tau|$. Therefore, the average is not necessarily a better estimate of the actual function but is an average of the variations in the limited set of data.

The values of $|\tau|$ thus obtained from density and transmission data are shown in Fig. 17. The function tends to be greater than 1 at most frequencies, which indicates a highly nonlinear process. The duplication factor goes above 1 in the region of 3 to 11 cycles/mm for each band. The same effect was reported by Simonds[27] for contact prints of grain patterns. Also, the upward trend of the functions has been attributed to Fresnel diffraction (a nonlinear phenomenon) within the emulsion layer.[25] The wide variation in the BB band cannot be explained but could be caused by marks and scratches on the film, which were most prominent in this band.

Linear noise filtering of second and fourth generation images (see SO65 MTF analysis and Appendix C) had little effect on the MTFs obtained, indicating that the modulation increase

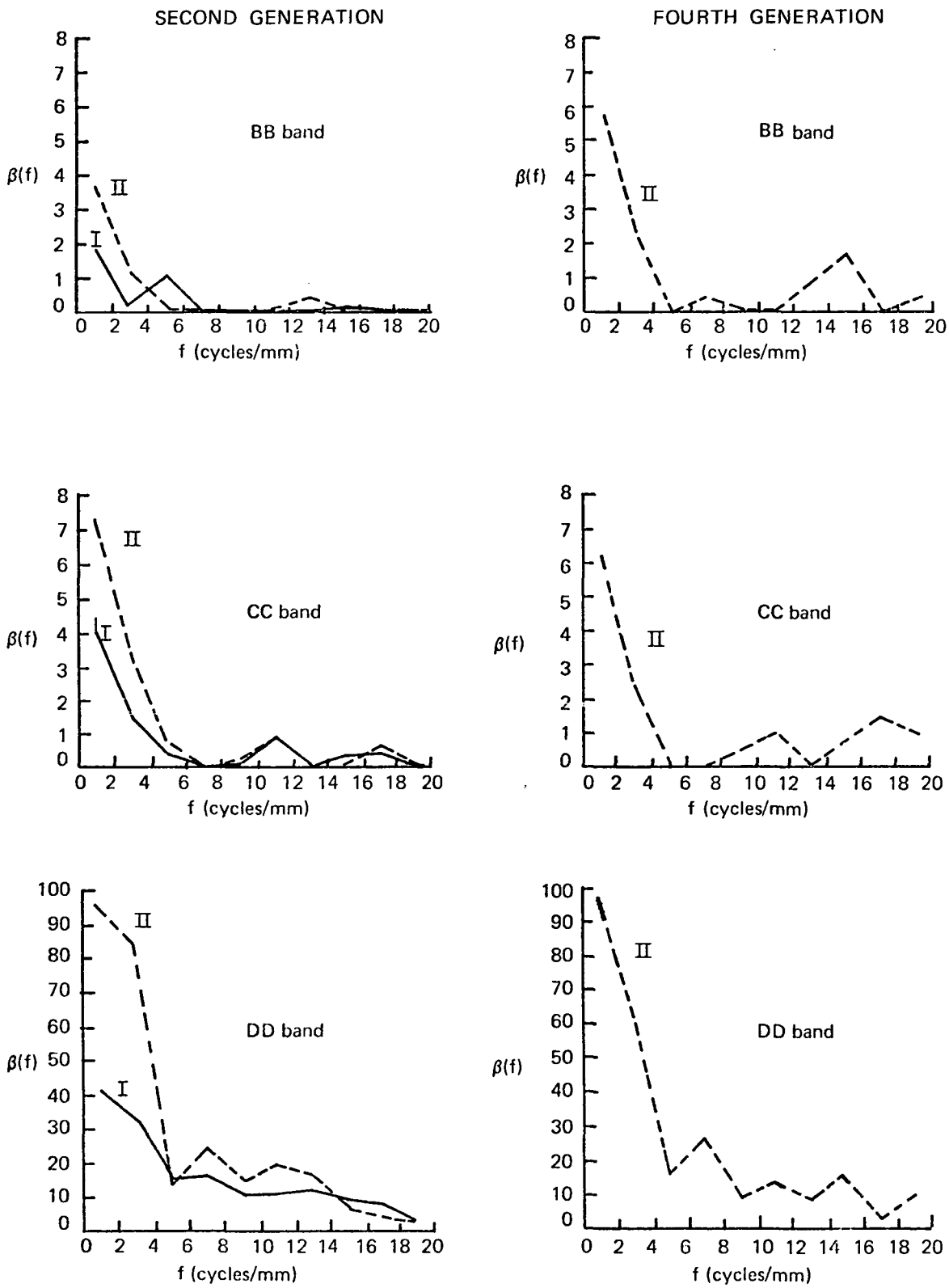

Fig. 16. Signal-to-noise ratios for second and fourth generations.

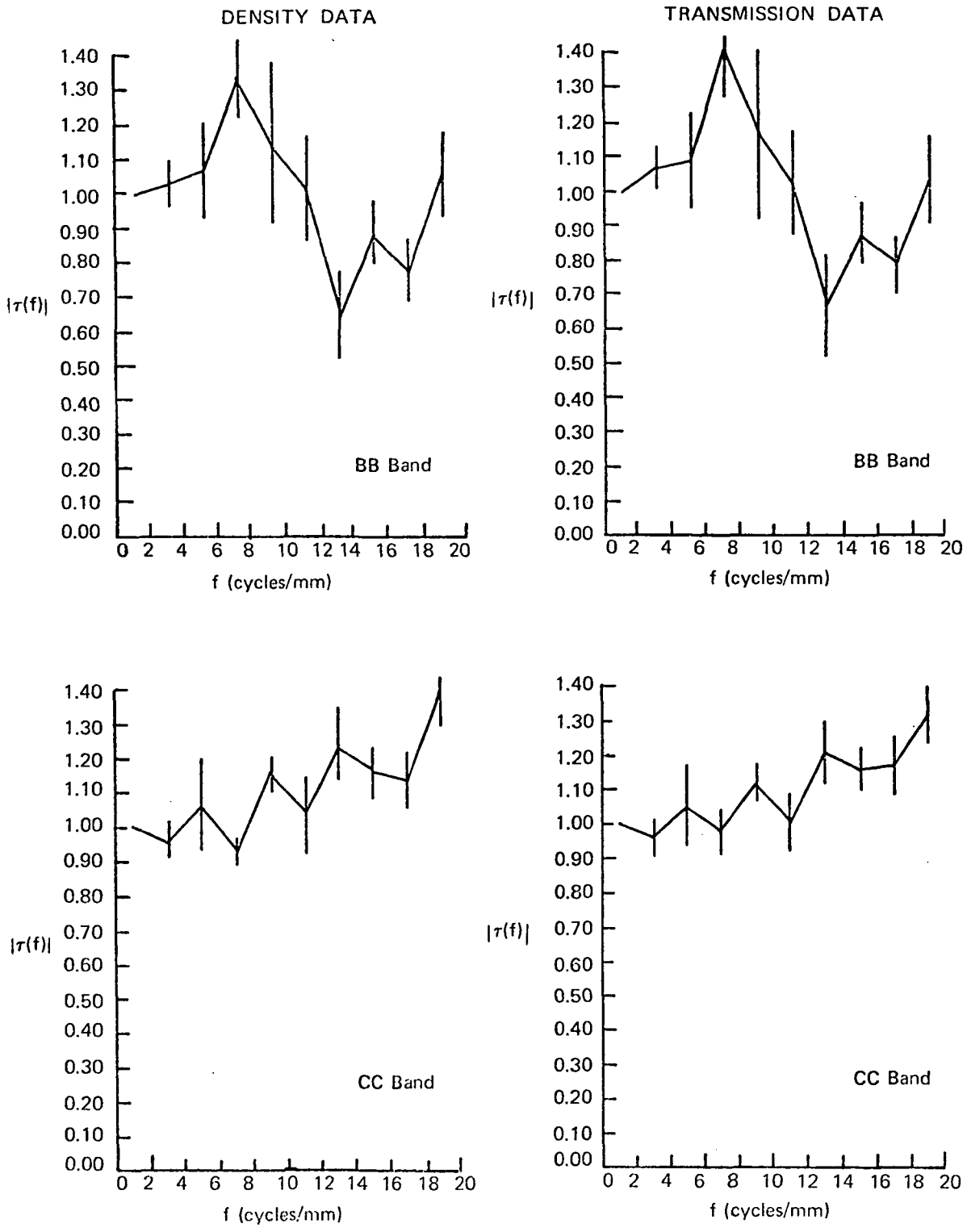

Fig. 17. MTF of duplication process.

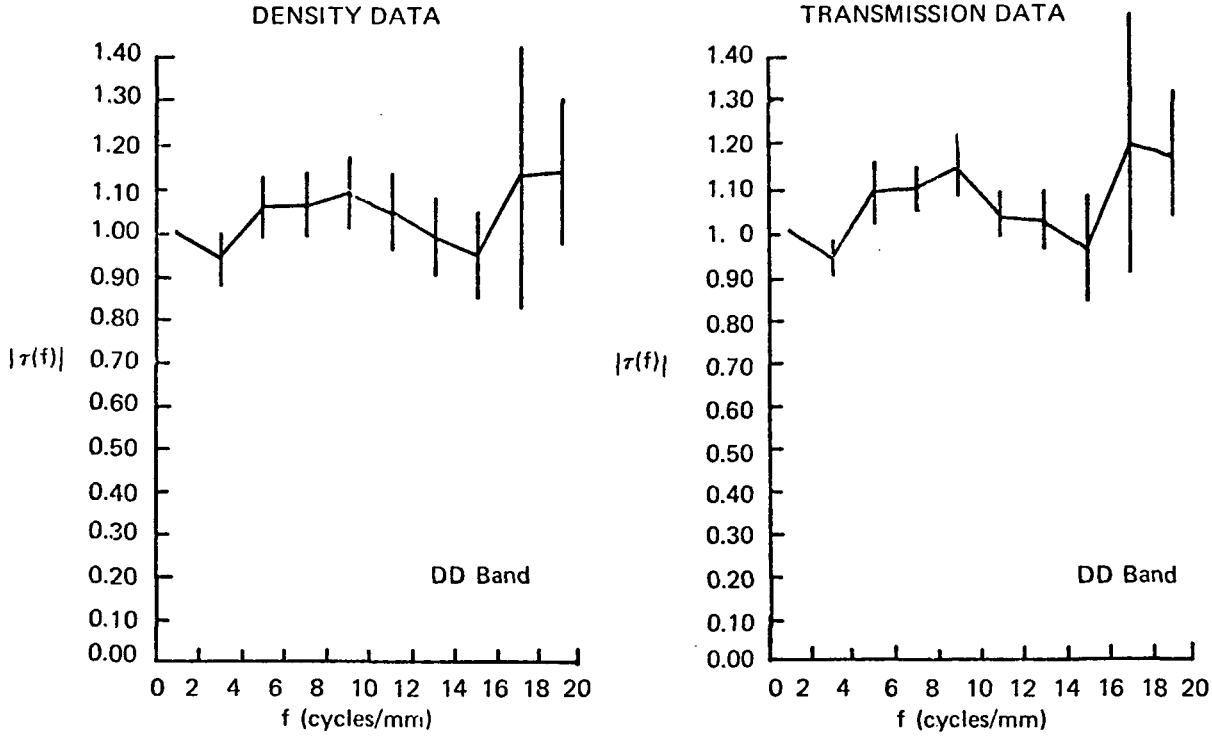

Fig. 17. (Continued).

is probably related to the duplication process and not to a granularity effect. Likewise, converting the fourth generation transmission values to effective exposure by using the over-all γs of the process (see Sensitometric Analysis) left the MTFs unchanged within 0.10. Indeed, if the logarithmic change from transmission to density produced the small changes in MTF in Fig. 17, we would not expect correction for γs to be significant.

Although these transfer curves seem to indicate an enhancement of the image, a comparison of the granularity change in duplication *at the mean density level of the corresponding image* shows a large increase in graininess. Figure 18 shows the standard deviation in density and transmission measurements of uniformly exposed film, developed to the *same* mean density of the image, as a function of the generation. These data were taken from Figs. 5 through 7 by linear interpolation. We see that

	Density	Transmission
BB	$\Delta\sigma_{24} = +38\%$	$\Delta\sigma_{24} = +48\%$
CC	$\Delta\sigma_{24} = +66\%$	$\Delta\sigma_{24} = +120\%$
DD	$\Delta\sigma_{24} = +41\%$	$\Delta\sigma_{24} = +108\%$

Again, the high density of the BB band keeps the change in σ (transmission) small relative to the other bands.

The increasing MTF curves are thus deceiving. Although there is an increase in image modulation, the fourth generation images may well appear lower in resolution when viewed in a microscope owing to the subjective and objective effects of increased granularity.

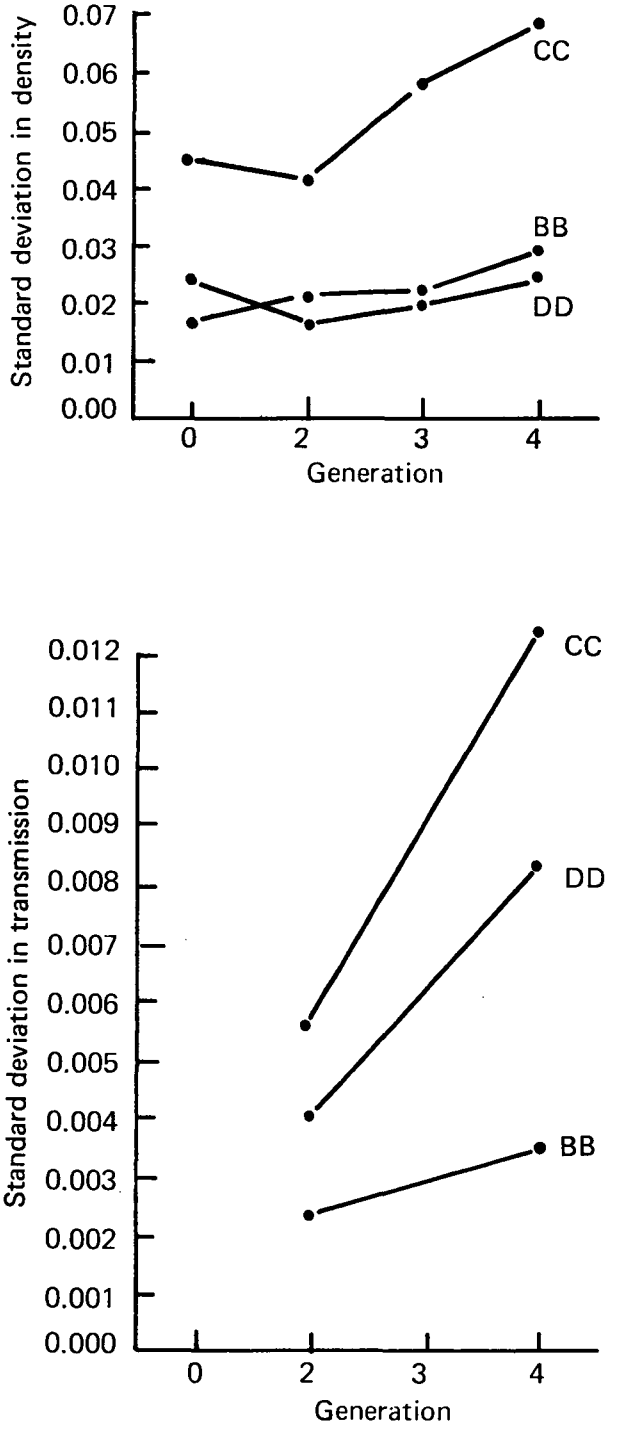

Fig. 18. Granularity (scaled) at image density as a function of generation.

Analysis of SO65 System MTF

The high-altitude (HA) photography was assumed to represent the object for the SO65 photography. For this to be absolutely true, the HA images should be corrected for MTF, distortion, and spectroradiometric characteristics of the HA system. However, these cameras were not calibrated, so we must assume the images are duplicates of the objects, which is probably reasonable for comparing them to the much higher altitude SO65 images. The spatial frequencies in the HA image are scaled geometrically by the ratio of SO65 altitude to HA altitude because both sets of photographs were taken with approximately the same focal length optics. Because the HA systems were above essentially all of the atmosphere, wavelength-dependent atmospheric scattering, which reduces modulation, is about the same as that seen from the spacecraft, and will thus cancel in the comparison.

The ratio of SO65 spectra to HA spectra then leaves only the SO65 system MTF

$$|\tau_{SO65}(f)| = [\phi_{SO65}(f)/\phi_{HA}(f)]^{1/2}$$

where $\phi_{HA}(f)$ has been scaled along the frequency axis to correspond to the change in altitude between images.

This scale factor was difficult to determine because we did not know the exact altitude and focal length of the HA system. Measurements with a precision measuring microscope determined the scale to be about 11. Locating ground points accurately was difficult in the grainy SO65 images and was the chief source of inaccuracy for the scale factor. Therefore, in the data analysis several scale factors that bracketed 11 were tried, and a scale of 10.8 seemed to give the most consistently reasonable values for $|\tau|$. For example, the area under $|\tau|$ often peaked for a scale factor of 10.8. In addition, the modulation in the third frequency band (4 to 6 cycles/mm) was usually less than or equal to that in the second frequency band (2 to 4 cycles/mm) for the scale of 10.8. We would not expect oscillations of $|\tau|$ at these low frequencies, as did occur for some other scale factors.

Another, more serious, difficulty is in locating the same ground point in the SO65 scan and the HA scan. The grain noise of the SO65 images introduces uncertainty in the exact position of an object point, as discussed in the section on theory. However, there were some prominent features in the DD band that could be referenced to the HA image. By comparing the BB and CC scans to the DD scan for both the SO65 and HA images, we were able to obtain reasonably accurate locations for a ground point(s) to allow comparison of the same data from object to image.

The HA spectra were scaled by merely dividing the sample interval by the scale factor to obtain the effective sample interval at the SO65 altitude. Because the scale was not a multiple of 2, this effective interval was not quite the same as that for the SO65 image. Thus different numbers of points were taken in each image in order to ensure coverage of the same ground area. Generally there were 410 HA data points and 378 (variable with scale factor) SO65 data points. After subtracting the mean, the data were placed in an array of 512 points with zeros filling the portion of the array not occupied by data. The complete array was then Fourier transformed.

When the $|\tau|$s were calculated it became immediately apparent that the SO65 data needed to be noise filtered to obtain smooth MTFs. The grain variance in each frequency interval of

the SO65 spectra caused oscillation of the MTF and produced values greater than 1. The HA scans were essentially noiseless because of the large aperture size used (0.22 X 0.99 mm) in this case.

Thus we derived a linear filter by using the Wiener mean-squared difference minimization procedure (see Appendix C). The filter was found to be

$$W(f) = 1/[1 + 1/\beta(f)]$$

and was applied to the spectra

$$[\phi_{SO65}(f)]^{1/2} = [\phi_{SO65}(f)]^{1/2}[W(f)].$$

This procedure improved the results greatly and made the problem of low signal-to-noise ratio more apparent. It was found that reasonable values for $|\tau|$could not be obtained for β less than approximately 2. Thus the BB and CC bands were necessarily eliminated from the MTF calculations. The DD band did possess sufficiently high β throughout the spectrum up to 20 cycles/mm to permit an MTF calculation. The curve in Fig. 19 is the MTF for this band. It is an average over the MTFs obtained from three sections of data within the scan, where the MTF from each section of data was the average over three adjacent starting points about the selected image point in the SO65 scan. This average over starting points counteracted the uncertainty in image position as explained above. However, there was very small change in the MTFs from different starting points. In addition, each MTF was averaged over three scale factors: 10.7, 10.8, and 10.9. There was some variation among these values, but the maximum and minimum values represented in Fig. 19 were primarily from variations between sections of data.

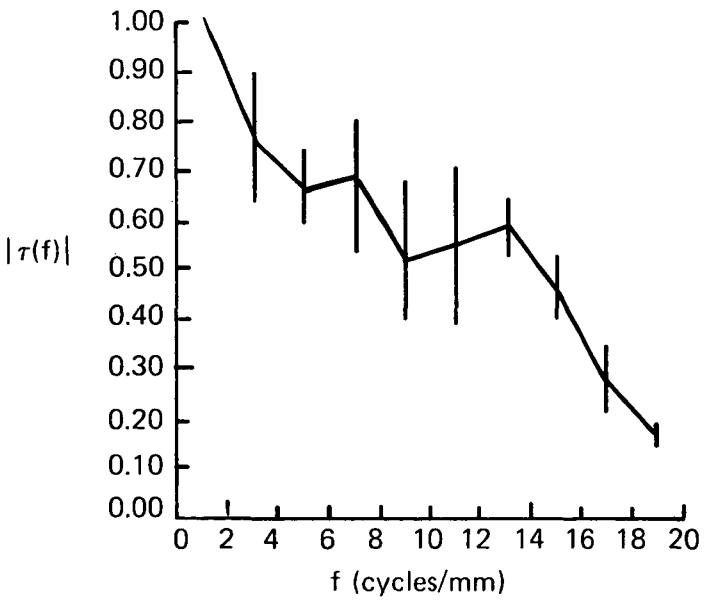

Fig. 19. MTF for DD band SO65 system.

Resolution Estimate for the DD Band

The estimation of three-bar resolution can be achieved with system MTF data and aerial image modulation (AIM) curves.[28] The MTF curve in Fig. 19 was divided by the MTF (in red light) for type 3400 film (Pan-X).[29] The AIM curve for this film was then superimposed on the MTF curve, as in Fig. 20. With extrapolation of the MTF curve, the three-bar resolution could be estimated to be about 20 lp/mm.

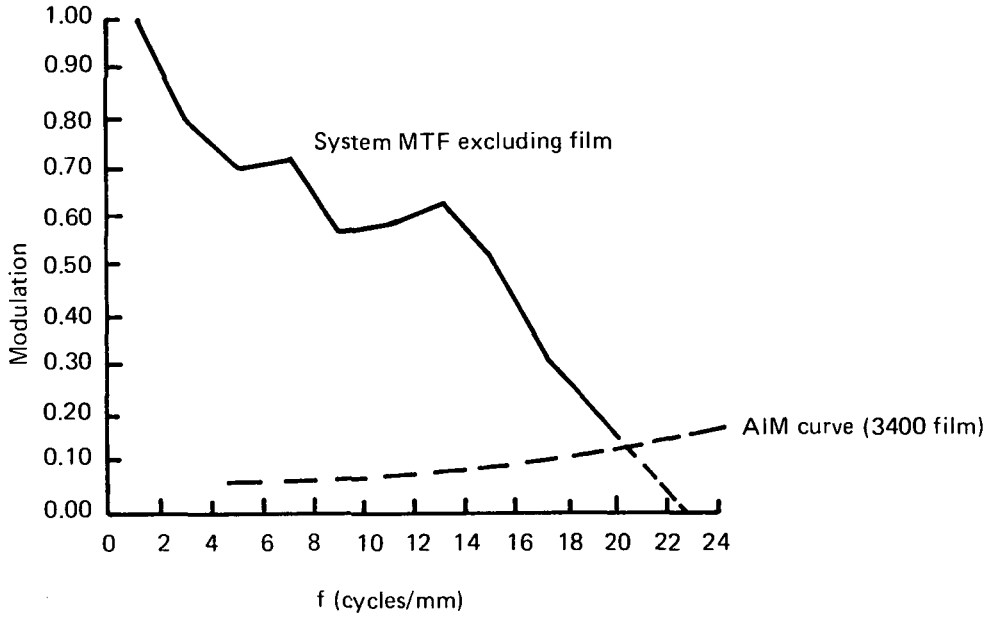

Fig. 20. Estimation of three-bar resolution for DD band SO65 system.

Recommendations

In this study we have used a new, convenient, technique for evaluating the image quality of space photographs and the degradation introduced into the imagery by duplication from generation to generation. The primary advantage of the technique is that it does not rely on specific targets in the image but uses the spatial spectrum of the natural scene.

This report has described the first attempt to employ this evaluation technique. It is appropriate to emphasize the special requirements with respect to calibration, sensitometry, microdensitometry, etc. that will improve the quality of the results obtained in future studies of this type.

(1) The quantities of fundamental interest are the intensity in a small region of the aerial image and the radiance of the corresponding area on the ground. This is a spectroradiometric problem that requires careful sensitometry of the proper type. The spectral characteristics of the ground vary considerably from frame to frame and even within a frame. Thus

we need some type of "real time" sensitometry in which the film densities are calibrated to image intensities for each particular ground scene. This may be accomplished, for example, by imaging the exit pupil of the optical system, which is uniformly irradiated, through a neutral density wedge onto a portion of each individual frame. The spectral nature of the irradiance used in the calibration will then be an average of that for the entire scene.

(2) As discussed earlier in this report, there was some difficulty in locating the same ground point in all the scans. In this study it was complicated by the fact that, because of variations in spectral reflectance, the object was different in each band. Some means of establishing a good ground reference point is necessary. In the absence of prominent man-made features, one solution may be to view the photographs in a microscope and mark the same ground point in each case with a scratch on the film. The scratch will then be plainly visible in the microdensitometer scan. A microdensitometer with more precise positioning capability than the Joyce-Loebl instrument would be desirable. Of course, because of the uncertainty in spatial position introduced by the film grain, there will always be a need to do some type of averaging over neighboring points, as was done in this work.

(3) The ground area selected should possess sufficient modulation in all bands to permit reliable MTF calculations. It may be necessary to select different ground scenes for the evaluation of each band because of the spectrally selective effect of atmospheric scattering and the spectral reflectance variation of the scene features.

(4) Corrections of the HA image for distortion, off-axis falloff in irradiation, and MTF of the optical system are necessary. Therefore, accurate data of this type must be available. For this study the lack of information about the HA system was not critical because of the low spatial frequencies studied, but to evaluate higher resolution orbital systems, calibration of the HA system to 10 or 15 cycles/mm will be necessary. It should be noted that the MTF measurements on the HA system should be made with spectral irradiances matching those in the spectral regions of each band in the space photography.

Appendix A – Functions and Operations

The functions and operations used in this report are defined as

$\mathrm{rect}(x/w)$

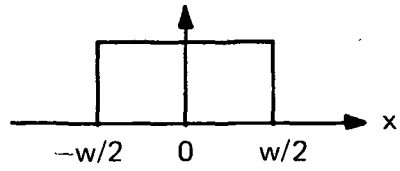

$\mathrm{sinc}(x/w) = \sin[\pi(x/w)]/[\pi(x/w)]$

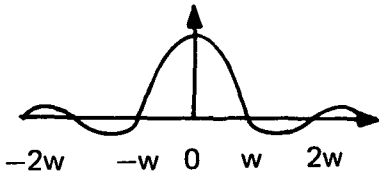

comb function $\text{Ш}(x/w) = \sum_{n=-\infty}^{\infty} \delta(x-nw)$

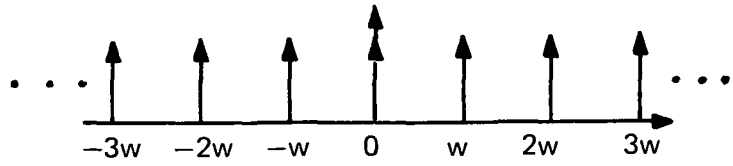

convolution $f(x) = g(x)*h(x) = \int_{-\infty}^{\infty} g(x')h(x-x')dx'$

cross correlation $C_{gh}(x) = g(x)\bigstar h(x) = \int_{-\infty}^{\infty} g(x')h\ (x+x')dx'$

autocorrelation $R_{gg}(x) = g(x)\bigstar g(x) = \int_{-\infty}^{\infty} g(x')g\ (x+x')dx'.$

Functions that are Fourier transform pairs are denoted by small and capital letters

$g(x) \longleftrightarrow G(f_x)$

The squared modulus is represented by ϕ

$\phi_G(f_x) = G(f_x)G^*(f_x).$

Appendix B – Mathematics of Scanning a Two-Dimensional Image

The image field is given by $i(x,y)$ and we choose a coordinate system aligned with the scan as shown in the figure below.

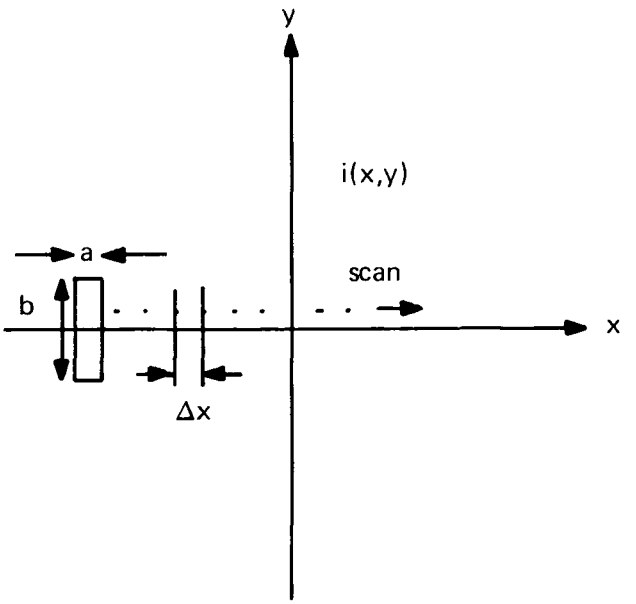

The scanning aperture is assumed rectangular with width a and length b, and it integrates over $i(x,y)$ for each data point. The data points are spaced Δx apart. Thus, at *each* data point, we have the value

$$d_n = \iint_{-\infty}^{\infty} \text{rect}[(x-n\Delta x)/a]\ \text{rect}(y/b)\ i(x,y)\ dxdy.$$

Since the rectangle is an even function, we have

$$d_n = \iint_{-\infty}^{\infty} \text{rect}[(n\Delta x-x)/a]\ \text{rect}(y/b)\ i(x,y)\ dxdy$$

$$= \int_{-\infty}^{\infty} \text{rect}(y/b)[\text{rect}(x/a)\ * i(x,y)]_{x=n\Delta x} dy.$$

Each data point is thus a value off the convolution curve of the aperture with the image. We assume that the integration time for each point is infinitesimal.

Interchanging the order of integration we can write

$$d_n = [\text{rect}(x/a) * \int_{-\infty}^{\infty} \text{rect}(y/b)\ i(x,y)dy]_{x=n\Delta x}.$$

We call the integral over y a new function of x alone

$$I(x) = \int_{-\infty}^{\infty} \text{rect}(y/b)\ i(x,y)\ dy \qquad (1)$$

and have

$$d_n = [\mathrm{rect}(x/a) * I(x)]_{x = n\Delta x}.$$

The total set of data is N points

$$d = \sum_{n=-N/2}^{N/2} d_n = \sum_{n=-N/2}^{N/2} \mathrm{rect}(n\Delta x/a) * I(n\Delta x)$$

$$= \text{Ш}(x/\Delta x)\,\mathrm{rect}(x/N\Delta x)[\mathrm{rect}(x/a) * i(x)]. \tag{2}$$

The Fourier transform of Eq. (2) is

$$D = \text{Ш}(f_x \Delta x) * \mathrm{sinc}(f_x N\Delta x) * [\mathrm{sinc}(f_x a) I(f_x)].$$

Thus the spectrum of the image, $I(f_x)$, is filtered by the aperture spectrum, smoothed by convolution with the narrow $\mathrm{sinc}(f_x N\Delta x)$ from the finite record length and replicated at intervals of $1/\Delta x$ by the comb function. Note that

$$N\Delta x \gg a.$$

The spectrum modulus is shown below diagrammatically.

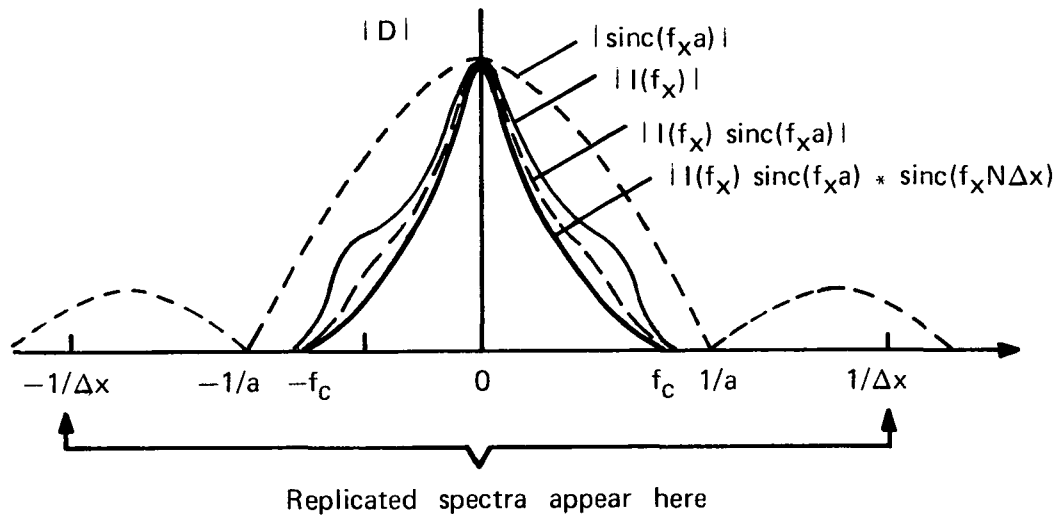

If $1/a = f_c$, we require, to avoid overlap of the spectra,

$$\Delta x \leqslant 1/2f_c = a/2$$

or at least two sample points within an aperture width. If, however, a is such that

$$f_c \leqslant 1/2a$$

or

$$a \leqslant 1/2f_c = P_c/2, \qquad P = \text{period},$$

the requirement is

$$\Delta x \leqslant a.$$

The situation corresponds to the slit width integrating over less than half the period of the highest frequency component as shown in the figure below. The result effectively corresponds to the ideal sampling theorem, where the function is sampled with delta functions.

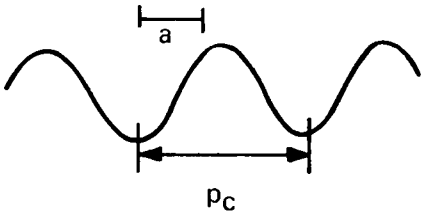

It is well known that the aerial image is band-limited and possesses a unique f_c. But, in general, the photographic image is not band-limited to f_c because of grain spectra that may extend far past f_c. If the noise spectra are significant past f_c, one must consider possible overlapping of the spectra. In this regard, note that the slit is filtering the spectra and reduces their magnitude considerably after the first zero.

Now let us return to Eq. (1)

$$I(x) = \int_{-\infty}^{\infty} \text{rect}(y/b)\, i(x,y)\, dy\ .$$

The image is the convolution of the object with the point spread function of the optical system. That is

$$I(x) = \int_{-\infty}^{\infty} \text{rect}(y/b)[o(x,y) \ast\ast s(x,y)]\ dy. \tag{3}$$

Suppose that the object is one-dimensional, e.g. an edge or line. Then

$$o(x,y) = o(x)$$

and

$$I(x) = o(x) * [\int_{-\infty}^{\infty} \text{rect}(y/b)\, s(x,y)\, dy] .$$

If the length of the slit is much greater than the characteristic (however defined) width of s, i.e.,

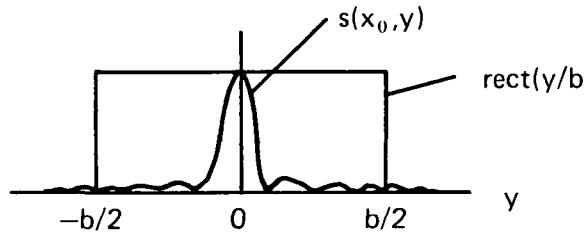

then

$$\int_{-\infty}^{\infty} \text{rect}(y/b)\, s(x,y)\, dy \approx \int_{-\infty}^{\infty} s(x,y)\, dy,$$

which is defined to be the line spread function for the optical system

$$l(x) \equiv \int_{-\infty}^{\infty} s(x,y)\, dy .$$

Thus

$$I(x) = o(x) * l(x)$$

and

$$I(f_x) = o(f_x)\tau(f_x)$$

where $\tau(f_x)$ is the transfer function profile along the f_x axis.

In aerial photography $o(x,y)$ is not usually one-dimensional. We must use Eq. (3) in its full form

$$I(x) = \int_{-\infty}^{\infty} \text{rect}(y/b)[o(x,y) ** s(x,y)]\, dy .$$

Now suppose the object (let the geometrical magnification from object to image be one) is bounded in the y direction by

$$o(x,y) = 0 \text{ for } |y| > b/2.$$

We are therefore ignoring contributions to the measured image (i.e., the radiant energy within the slit) from the convolution of the spread function with object points outside the

slit in the y direction. Then

$$I(x) = \int_{-\infty}^{\infty} \text{rect}(y/b)[o(x,y/b)**s(x,y)]dy.$$

If we now assume that the rect(y/b) function includes essentially all of the radiant energy in the y direction of the image, i.e.,

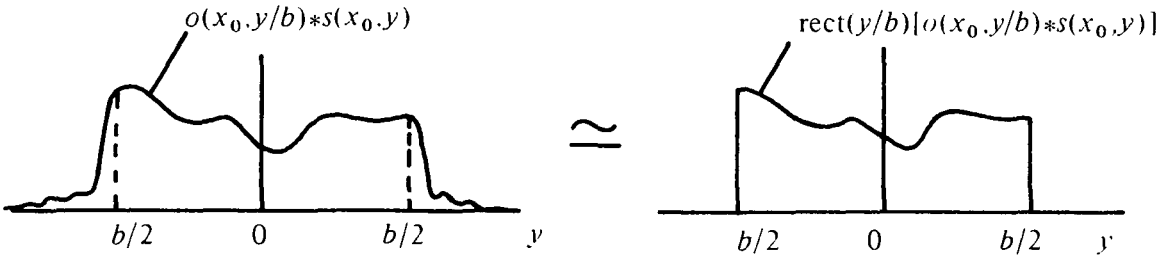

we can say

$$I(x) \approx \int_{-\infty}^{\infty} o(x,y/b)**s(x,y)dy.$$

By the properties of Fourier transforms

$$F_x[I(x)] = F_x[\int(\text{integrand})dy] = F_{xy}(\text{integrand})\,|_{f_y=0}.$$

From above

$$F_x[I(x)] \approx o(f_x,o)\tau(f_x,o)$$

which again gives the profile of $\tau(f_x,f_y)$ along the f_x axis. Note that the two assumptions used to achieve this result essentially require that the slit length b be much greater than the width of $s(x,y)$ in the y direction and that the object not increase rapidly in radiance for points in the vicinity of $y = \pm b/2$. The last assumption is valid for low-contrast aerial and space photography.

Appendix C – Derivation of the Wiener Filter for a Noisy Image

We assume the photographic image is given by the sum of the aerial image and *independent, uncorrelated* noise with zero mean

$$i_m(x) = i(x) + n(x), \ \langle n(x) \rangle = 0.$$

We wish to estimate $i(x)$ in a reasonable way. Calling the estimate $\hat{i}(x)$, we will use the criterion that the mean squared error between the functions $i(x)$ and $\hat{i}(x)$ is a minimum over all x. That is,

$$\left\langle \int_{-\infty}^{\infty} |i(x) - \hat{i}(x)|^2 dx \right\rangle = \text{minimum.} \tag{4}$$

Now to obtain the image estimate let us find a *linear* filter that operates on the measured image, i_m, so that the above equation is true. We assume

$$\hat{i}(x) = w(x) * i_m(x).$$

Carrying out the square in Eq. (4), we have

$$\int_{-\infty}^{\infty} [\langle |i|^2 \rangle + ww^* * \langle |i_m|^2 \rangle - w^* \langle i i_m^* \rangle - w \langle i^* i_m \rangle] dx = \text{minimum}$$

$$= \int_{-\infty}^{\infty} [R_i + ww^* * R_{i_m} - w^* C_{ii_m} - w C_{i_m i}] dx$$

where R is the autocorrelation and C is the cross correlation (see Appendix A).

Now

$$C_{ii_m} = \langle i i_m^* \rangle = \langle i(i^* + n^*) \rangle = \langle |i|^2 \rangle + \langle i n^* \rangle.$$

Since the noise is uncorrelated with the image and has zero mean,

$$\langle i n^* \rangle = \langle i \rangle \langle n^* \rangle = 0$$

and $C_{ii_m} = R_i$. Similarly, $C_{i_m i} = R_i$.

Thus, the requirement is

$$\int_{-\infty}^{\infty} [R_i + ww^* * R_{i_m} - w^* R_i - w R_i] dx = \text{minimum.}$$

To find w, differentiate the above equation with respect to w^* at each x (differentiation with respect to w will just result in the solution for w^*) and set the result equal to zero. Then

$$w * R_{i_m} - R_i = 0.$$

Taking the Fourier transform,

$$W\phi_{i_m} - \phi_i = 0$$

or

$$W = \phi_i/\phi_{i_m} \quad \text{(note } W \text{ is real and positive).}$$

Now,

$$R_{i_m} = R_i + R_n + \langle in^* \rangle + \langle i^* n \rangle = R_i + R_n.$$

Thus,

$$\phi_{i_m} = \phi_i + \phi_n$$

and

$$W = \phi_i/(\phi_i+\phi_n) = 1/[1+(1/\beta)], \ \beta = \text{signal-to-noise ratio.}$$

A plot of W as a function of β is shown below. This filter is increasingly effective as the signal-to-noise ratio decreases, as it should be, and approaches unity asymptotically as β increases.

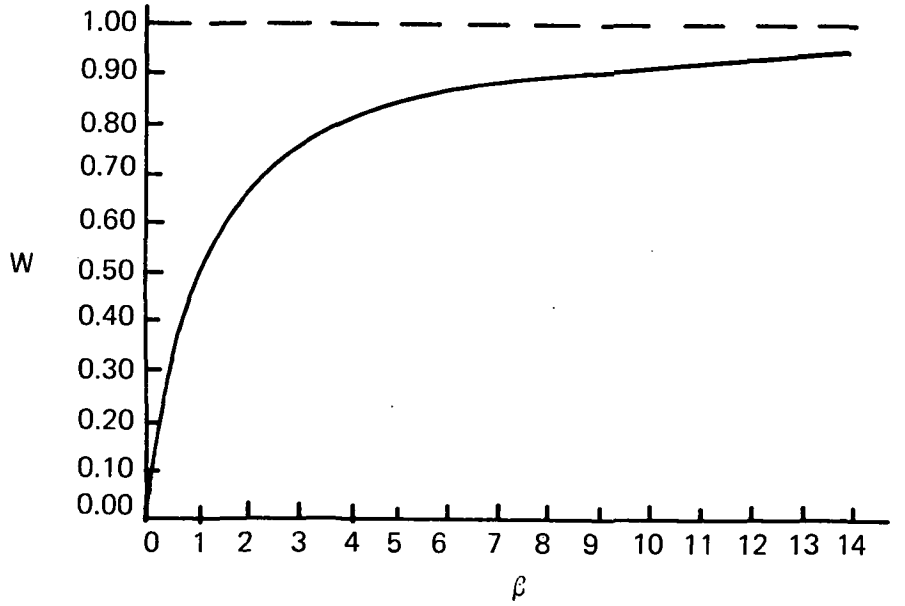

Appendix D – Some Properties of the Imagery

The SO65 frame and HA frame are shown plotted on map coordinates in Fig. 20. The points 3785 and 3786 are the principal points for the respective frames, and the line joining their centers is assumed to be the direction of the spacecraft velocity. The velocity of the underflight was almost perpendicular to the spacecraft's velocity. Also note that the image scan is essentially parallel to the aircraft velocity and perpendicular to the spacecraft velocity. Thus the HA image spectrum will include the effect of image motion while the SO65 image spectrum will not. However, as shown below, the image motion in the HA image was negligible.

Very little background information was available for the HA imagery. The following values are reasonable assumptions:

HA Image

focal length f_{HA} = 80 mm (camera was specified as a Vinten using 70-mm film)
aircraft velocity $v_{HA} \approx$ 450 mph
aircraft altitude $H_{HA} \approx$ 70,000 feet (U-2 aircraft)
shutter speed $t_{HA} \approx$ same as the SO65 cameras
image motion $\Delta_{HA} = f_{HA}(v_{HA}/H_{HA})t_{HA}$

	BB	CC	DD
t_{HA} (sec)	0.008	0.004	0.004
Δ_{HA} (mm)	0.006	0.003	0.003

The values for Δ_{HA} are rather low and certainly do not affect the image at the spatial frequencies of interest (0 to 2 cycles/mm).

SO65 Image

f_{SO65} = 80 mm (Hasselblad cameras, 80-mm Zeiss Planar lens)
$v_{SO65} \approx$ 25,000 ft/sec
$H_{SO65} \approx$ 126 nautical miles
$\Delta_{SO65} = f_{SO65}(v_{SO65}/H_{SO65})t_{SO65}$

	BB	CC	DD
t_{SO65} (sec)	0.008	0.004	0.004
Δ_{SO65} (mm)	0.021	0.010	0.010

Thus the spacecraft imagery was subject to considerable linear image motion because the image motion MTF had a cutoff frequency of about 50 cycles/mm for the BB band. In the analysis discussed in this report, however, the image motion was not a factor because the image scan was almost perpendicular to it. The above calculation does, however, point out the need for linear image motion compensation in orbital systems as is being incorporated in the S190 photographic experiment on Skylab.

The average modulation of the object scene *after transmission by the atmosphere* was calculated for each band from the HA scan. If one defines modulation in terms of irradiance as

$$M = (I_{\max} - I_{\min})/(I_{\max} + I_{\min}) = (I_{\max} - I_{\min}/2)/(I_{\max} + I_{\min}/2)$$

it can be seen that an average rms modulation for an arbitrary object can be given by the ratio of the standard deviation to the mean.

$$\bar{M} = \sigma/\bar{I}.$$

$\bar{M}$ was calculated from the transmission data of the HA scan and is shown below for each band. $\bar{C}$ is the rms contrast and equals $(1+\bar{M})/(1-\bar{M})$.

	BB	CC	DD
$\bar{M}$	0.10	0.12	0.15
$\bar{C}$	1.2	1.3	1.4

The scenes generally possess low modulation and contrast when seen through the atmosphere. As expected, the effect of atmospheric scattering is greatest for the green (BB) band. The low modulation is typical of aerial photography and is the chief cause of the low signal-to-noise ratios reported in earlier sections of this paper.

Distortion of the HA image in the scanned region owing to the elevation variations on the ground was negligible. According to topographic maps of the area, the maximum elevation change, ΔH, from the endpoint to the center of the scan line was about

$$\Delta H \leqslant 100 \text{ feet.}$$

Using the photogrammetrist's formula[30] for the change in image position

$$\Delta y = y\Delta H/H$$

where y is the distance from the center of the format, and H is the altitude of the aircraft. We obtain

$$\Delta y = 0.019 \text{ mm}$$

for the maximum distortion from this case. It is much less than the slit width and is on the order of two sample intervals.

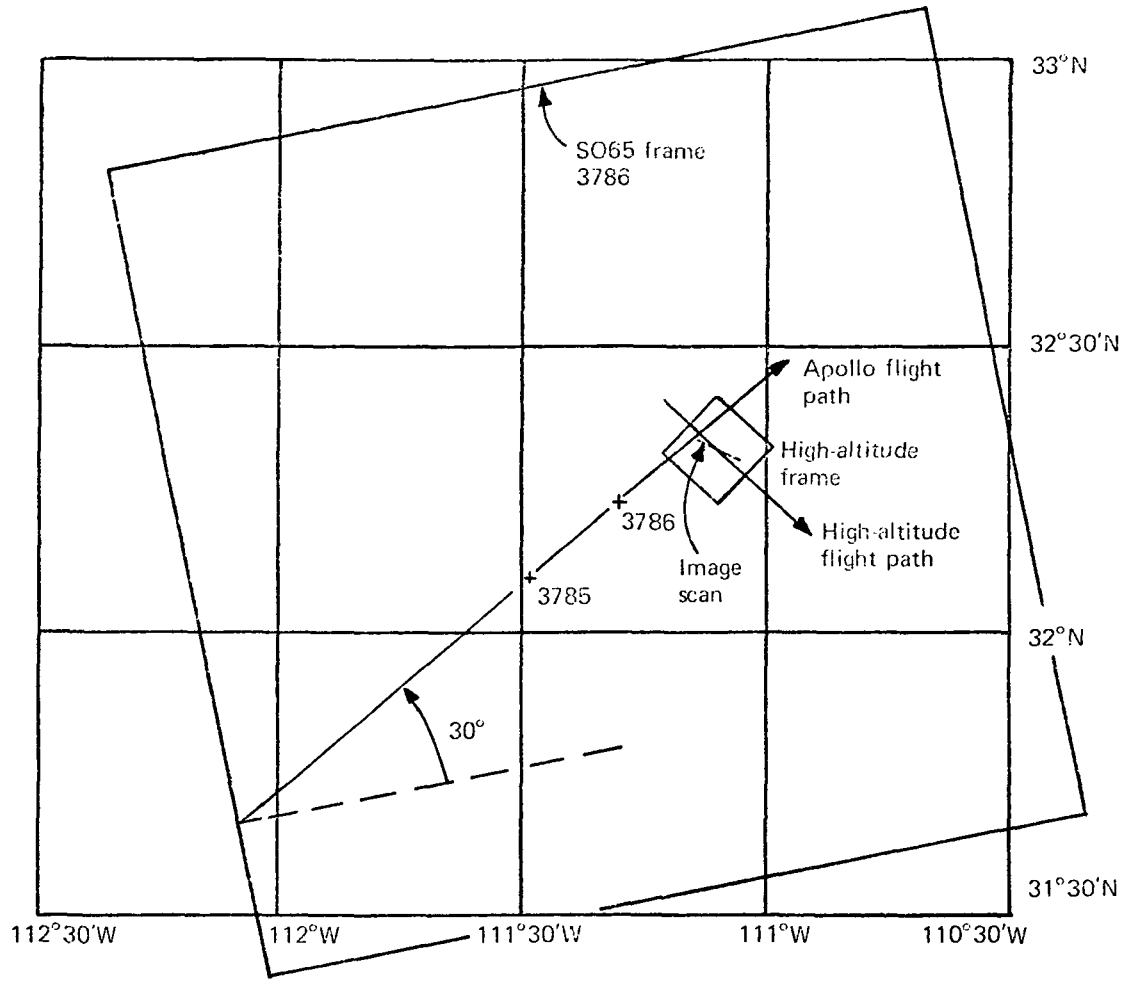

Fig. 20. Geometry of spacecraft and high-altitude photography.

Acknowledgments

We wish to thank the staff of the Photographic Technology Laboratory for its assistance in providing the photographic imagery and associated sensitometry. We are grateful to Sherman S. C. Wu of the U.S. Geological Survey in Flagstaff, Arizona, for providing the use of a microdensitometer. Thanks also go to Peter Keenan of the Optical Sciences Center who initiated the work here on Wiener spectra and who has remained interested in the analysis throughout the program and to Dr. Ronald S. Hershel, a recent graduate of the Optical Sciences Center, who supplied and perfected the fast Fourier transform algorithm used in this work.

All work reported here was conducted under contract NAS 9-9333, "Post-Flight Analysis and Calibration of Camera System for Apollo Experiment SO65," from the Manned Spacecraft Center, Houston, Texas. Mr. G. L. Kraus was the technical monitor on the contract.

References

[1] P. B. Keenan and P. N. Slater, "Preliminary post-flight calibration report on Apollo 9 multiband photography experiment SO65," Optical Sciences Center Technical Memorandum 1, September 1969.

[2] P. B. Keenan, R. A. Schowengerdt, and P. N. Slater, "Interim post-flight calibration report on Apollo 9 multiband photography experiment SO65," Optical Sciences Center Technical Memorandum 2, June 1970, pp. 11-12.

[3] R. A. Schowengerdt and P. N. Slater, "Interim post-flight calibration report on Apollo 9 multiband photography experiment SO65," NASA contract NAS 9-9333, June 1971.

[4] E. L. O'Neill, *Introduction to Statistical Optics*, Reading, Mass., Addison-Wesley, 1963.

[5] R. G. Musgrove, "Photometry for interpretation," Photogrammetric Eng. 35(10):1015-1023, October 1969.

[6] R. Welch, "Analysis of image definition," Photogrammetric Eng. 35(12):1228-1238, December 1969.

[7] L. O. Hendeberg and E. Welander, "Experimental transfer characteristics of image motion and air conditions in aerial photography," Appl. Opt. 2(4):379-386, April 1963.

[8] J. J. Sikora, "Modulation transfer function using a modified dirac comb target," Data Corporation Technical Note DTN-70-5, August 1971.

[9] J. J. Sikora, "Two dimensional system analysis," Data Corporation Technical Note DTN-70-7, August 1971.

[10] R. A. Jones and E. C. Yeadon, "Determination of the spread function from noisy edge scans," Photog. Sci. Eng. 13(4):200-204, July-August, 1969.

[11] R. A. Jones, "An automated technique for deriving MTFs from edge traces," Photog. Sci. Eng. 11(2):102-106, March-April 1967.

[12] F. Scott, R. M. Scott, and R. V. Shack, "The use of edge gradients in determining modulation transfer functions," Photog. Sci. Eng. 7(6):345-349, November-December 1963.

[13] J. D. Finley and W. W. Marshall, "Image assessment research," Data Corporation Final Report, 1965.

[14] R. Bracewell, *The Fourier Transform and Its Application*, New York, McGraw-Hill, 1965, p. 9.

[15] R. B. Blackman and J. W. Tukey, *The Measurement of Power Spectra*, New York, Dover Press, 1959, p. 176.

[16]R. J. Arguello, "Encoding, transmission and decoding of sampled images," in *A Symposium on Sampled Images*, Perkin-Elmer, 1971.

[17]J. L. Simonds, "Analysis of nonlinear photographic systems," Photog. Sci. Eng. 9(5):294-300, September-October 1965.

[18]J. G. Thunen, "Signal processing in the presence of signal-dependent noise," Optical Sciences Center Technical Report 65, 15 March 1971.

[19]R. Bracewell, *The Fourier Transform and Its Application*, New York, McGraw-Hill, 1965, p. 194.

[20]E. C. Doerner, "Wiener-spectrum analysis of photographic granularity," J. Opt. Soc. Am. 52(6):669-672, June 1962.

[21]R. E. Kinzly, "Partially coherent imaging in a microdensitometer," J. Opt. Soc. Am. 62(3):386-394, March 1972.

[22]W. N. Charman, "Some experimental measurements of diffraction images in low-resolution microscopy," J. Opt. Soc. Am. 53(4):410-419, April 1963.

[23]Eastman Kodak Company, "Characteristics of Kodak aerial films," Tech Bits 2, Eastman Kodak Company, Rochester, New York, 1968.

[24]E. A. Trabka, "Crowded emulsions: granularity theory for monolayers," J. Opt. Soc. Am. 61(6): 800-810, June 1971.

[25]R. A. Jones and G. C. Trinks, "Near field diffraction in contact printing," Appl. Opt. 10(7):1659-1663, July 1971.

[26]C. E. K. Mees and T. H. James, *The Theory of the Photographic Process*, Third Edition, New York, Macmillan, 1966, p. 421.

[27]J. L. Simonds, "Reproduction of fine structure in photographic printing. II. Spatial interactions of the development process," Photog. Sci. Eng. 8(3):174-177, May-June 1964.

[28]F. Scott, "Three-bar target modulation detectability," Photog. Sci. Eng. 10(1):49-52, January-February 1966.

[29]Eastman Kodak Company, "Modulation transfer data for Kodak films," Kodak Pamphlet P-49, Third Edition, September 1967.

[30]M. M. Thompson, ed., *Manual of Photogrammetry*, Vol. 1, Third Edition, American Society of Photogrammetry, p. 21, 1965.